

1 **Comparison of model and ground observations finds snowpack and blowing snow aerosols both**
2 **contribute to Arctic tropospheric reactive bromine**

3 William F. Swanson¹, Chris D. Holmes², William R. Simpson¹, Kaitlyn Confer³, Louis Marelle^{4,5}, Jennie
4 L. Thomas⁴, Lyatt Jaeglé³, Becky Alexander³, Shuting Zhai³, Qianjie Chen⁶, Xuan Wang⁷, Tomás
5 Sherwen^{8,9}

6 ¹Department of Chemistry and Biochemistry and Geophysical Institute, University of Alaska Fairbanks,
7 Fairbanks, Alaska

8 ²Department of Earth, Ocean and Atmospheric Science, Florida State University, Tallahassee, Florida

9 ³Department of Atmospheric Sciences, University of Washington, Seattle, Washington

10 ⁴Institut des Géosciences de l'Environnement (IGE), Institut Polytechnique de Grenoble, Grenoble, France

11 ⁵Laboratoire Atmosphères Observations Spatiales (LATMOS), Sorbonne Université, Paris, France

12 ⁶Department of Civil and Environmental Engineering, Hong Kong Polytechnic University, Hong Kong,
13 China

14 ⁷School of Energy and the Environment, City University of Hong Kong, Hong Kong, China

15 ⁸National Centre for Atmospheric Science, University of York, York, UK.

16 ⁹Department of Chemistry, University of York, York, United Kingdom

17 *Correspondence to:* William F. Swanson (wswanson3@alaska.edu)

18 **Abstract**

19 Reactive halogens play a prominent role in the atmospheric chemistry of the Arctic during
20 springtime. Field measurements and modeling studies suggest that halogens are emitted to the atmosphere
21 from snowpack and reactions on wind-blown snow-sourced aerosols. The relative importance of
22 snowpack and blowing snow sources is still debated, both at local scales and regionally throughout the
23 Arctic. To understand implications of these halogen sources on a pan-Arctic scale, we simulate Arctic
24 reactive bromine chemistry in the atmospheric chemical transport model GEOS-Chem. Two mechanisms
25 are included: 1) a blowing snow sea salt aerosol formation mechanism and 2) a snowpack mechanism
26 assuming uniform molecular bromine production from all snow surfaces. We compare simulations
27 including neither mechanism, each mechanism individually, and both mechanisms to examine conditions
28 where one process may dominate or the mechanisms may interact. We compare the models using these
29 mechanisms to observations of bromine monoxide (BrO) derived from multiple-axis differential optical
30 absorption spectroscopy (MAX-DOAS) instruments on O-Buoy platforms on the sea ice and at a coastal
31 site in Utqiagvik, Alaska during spring 2015. Model estimations of hourly and monthly average BrO are
32 improved by assuming a constant yield of 0.1% molecular bromine from all snowpack surfaces on ozone
33 deposition. The blowing snow aerosol mechanism increases modeled BrO by providing more bromide-

34 rich aerosol surface area for reactive bromine recycling. The snowpack mechanism led to increased model
35 BrO across the Arctic Ocean with maximum production in coastal regions, whereas the blowing snow
36 aerosol mechanism increases BrO in specific areas due to high surface wind speeds. Our uniform
37 snowpack source has a greater impact on BrO mixing ratios than the blowing snow source. Model results
38 best replicate several features of BrO observations during spring 2015 when using both mechanisms in
39 conjunction, adding evidence that these mechanisms are both active during the Arctic Spring. Extending
40 our transport model throughout the entire year leads to predictions of enhanced fall BrO that are not
41 supported by observations.

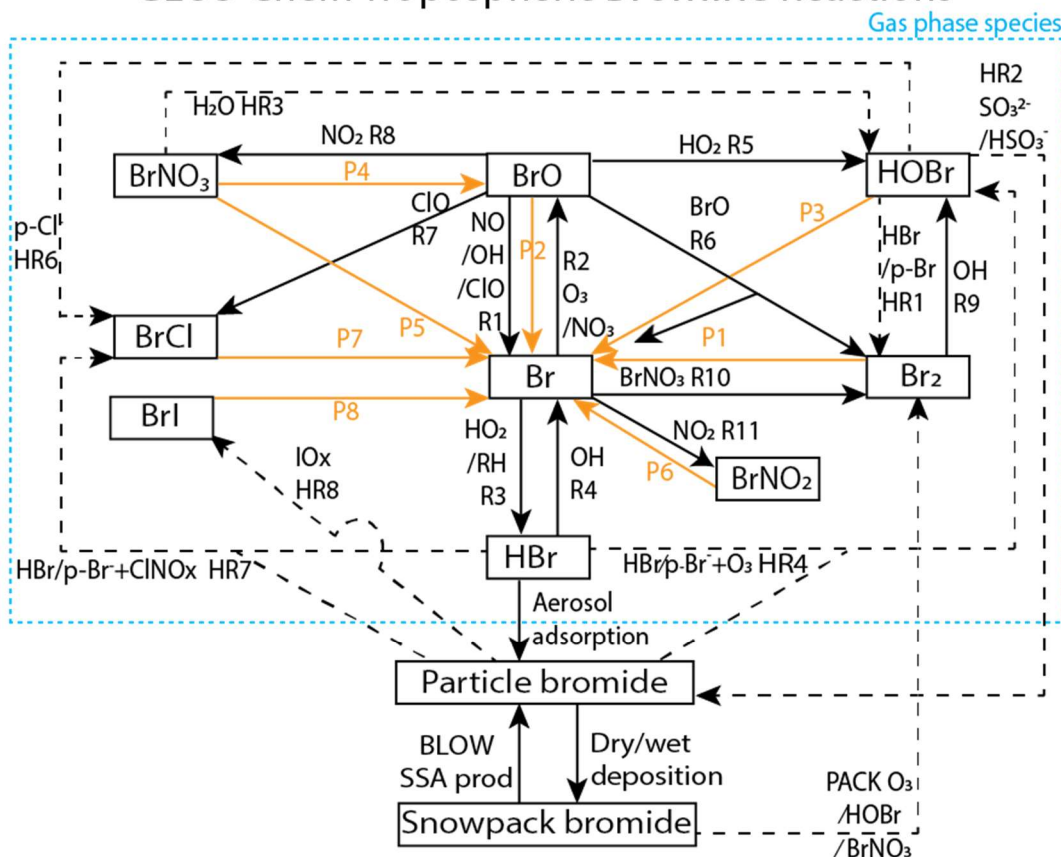
42 **1. Introduction**

43 Simulating Arctic halogen chemistry is a persistent problem for global models because processes
44 appear to differ between the Arctic and middle latitudes (Parrella et al., 2012; Schmidt et al., 2016).
45 Space-based instruments observe large column densities of reactive bromine across swaths of the Arctic
46 Ocean during the Arctic spring (Chance, 1998; Richter et al., 1998; Wagner and Platt, 1998). Increased
47 levels of tropospheric reactive bromine are associated with ozone depletion events (Barrie et al., 1988;
48 Foster et al., 2001; Koo et al., 2012; Halfacre et al., 2014) as well as oxidation of gaseous elemental
49 mercury (Schroeder et al., 1998; Nghiem, 2013; Moore et al., 2014). Bromine radicals have been
50 observed to lead directly to ozone depletion and mercury oxidation (Wang et al., 2019a). Deposition of
51 oxidized mercury to the snowpack can have deleterious effects on the health of Arctic humans and
52 animals (AMAP, 2011). Arctic reactive bromine chemistry impacts tropospheric oxidative chemistry but
53 is not typically accounted for in global models. Model studies have found that reactive halogen chemistry
54 can explain the oxidation of gaseous elemental mercury (Holmes et al., 2010) and reduce radiative forcing
55 from ozone (Sherwen et al., 2016c). Replicating reactive halogen chemistry in models requires inclusion
56 of multi-phase chemical reactions as well as mechanisms affecting sea salt aerosol particle production and
57 chemical reactions within the snowpack.

58 These increased levels of tropospheric reactive bromine radicals are a product of heterogeneous
59 photochemical reactions at the interface between air and saline surfaces such as surface snowpack and sea
60 salt aerosols (Saiz-Lopez and von Glasow, 2012; Simpson et al., 2015). Figure 1 depicts the gas-phase,
61 heterogeneous, and photochemical reactions thought to control tropospheric bromine, all of which are
62 included in the model and results presented in this manuscript. Bromine radicals (Br) are produced by
63 photolysis of molecular bromine (P1) or by self-reaction of BrO (R6) and react with ozone to form
64 bromine monoxide (BrO) (R2). Under sunlit conditions, BrO is most often photolyzed back to Br
65 radicals and an oxygen atom (P2) that then most often reforms ozone, resulting in a null cycle. Due to this
66 rapid interchange of Br and BrO, these two compounds form the BrO_x family. If processes other than BrO

67 photolysis (P2) convert BrO back to Br without producing ozone, the imbalance between these other
68 processes and P2 result in net ozone depletion. For example, ozone is depleted through R6 or R7 when
69 BrO reacts with another halogen oxide to form either Br₂ or BrCl, or through other more extended
70 processes. A reactive halogen activating cycle occurs when a BrO radical reacts with a hydroperoxy
71 (HO₂) radical in R5 to form gaseous hypobromous acid (HOBr). Heterogeneous chemistry can occur on a
72 saline surface between HOBr and particulate bromide (p-Br⁻) in HR1 forming Br₂ or particle chloride (p-
73 Cl⁻) in HR6 forming BrCl. For each cycle of reactions P1, R2, R5, and HR1, one hydroperoxy radical is
74 removed from the atmosphere, one bromine atom is released to the atmosphere, and one ozone molecule
75 is destroyed. This process of activation of particulate and snow bromide to Br₂ by consuming other
76 radicals (e.g. HO₂) is known as the "bromine explosion" (Wennberg, 1999). Ground-based instruments
77 have observed sharp increases in reactive bromine levels over the course of a single day from below 2
78 pmol/mol up to a maximum of 41 pmol/mol (Pöhler et al., 2010). Reactions may also sequester reactive
79 bromine into more stable bromine reservoir species. BrO may react with nitrogen dioxide (NO₂) in R8 to
80 form bromine nitrate (BrNO₃), which can also undergo hydrolysis on aqueous and ice surfaces to form
81 HOBr as in HR3.

GEOS-Chem Tropospheric Bromine Reactions



82
 83 **Figure 1: GEOS-Chem tropospheric bromine reactions.** Tropospheric bromine reservoirs shown in
 84 black boxes, with attached lines indicating reactions. Solid black lines R1-R11 indicate gas phase
 85 chemical reactions, solid orange lines P1-P8 indicate photolysis reactions, and dashed black lines HR1-
 86 HR8 indicate heterogeneous reactions. All gaseous species may undergo dry deposition. Additional
 87 sources of tropospheric bromine include the production of particulate bromide by the BLOW mechanisms
 88 and the production of Br₂ by the PACK mechanism, as well as the degradation of organobromines to form
 89 Br (OR1). Table 3 enumerates the specific species involved in each equation and shows reaction rates for
 90 each respective equation.

91 A potentially important competitor for recycling of reactive bromine through HOBr is its reaction
 92 with sulfur (IV) species, such as the reaction between HSO₃⁻ and HOBr in HR2 (Chen et al., 2017). To
 93 the extent that this reaction competes with HR1, it can slow the release of bromide from surfaces and
 94 reduce gas-phase reactive bromine (e.g., reduce BrO). Deposition of the HBr formed from HOBr by HR2
 95 can remove reactive bromine from the troposphere. In general, the termination of this chemistry leads to
 96 formation of HBr, which undergoes gas-particulate uptake to particulate bromide (p-Br⁻).

97 Ozone deposited to a saline surface can oxidize Br⁻ to form HOBr (similar to p-Br⁻ reactions
98 HR4a and HR4b) which is then converted to Br₂ or another dihalogen (e.g., BrCl). Production of reactive
99 bromine during ozone deposition does not require light and can occur at night (Oum et al., 1998; Artiglia
100 et al., 2017). The production of Br₂ is increased at low pH levels (Halfacre et al., 2019).

101 We define the inorganic bromine family, Br_y, in this manuscript as the sum of the bromine
102 species: Br, BrO, HOBr, BrNO₃, 2xBr₂, BrCl, BrI, and HBr, excluding p-Br⁻. The release of bromine from
103 sea salt aerosol particles was found to be the dominant global source of reactive bromine (Sander et al.,
104 2003; Zhu et al., 2019). Sea salt aerosol particles (SSA) sourced from the bursting of bubbles in oceanic
105 whitecaps and other sources and are one of the most abundant aerosol particle types present in the
106 troposphere (De Leeuw et al., 2011). Due to their abundance, SSA particles greatly increase the
107 particulate bromide on aerosol surfaces available for heterogeneous reactive bromine chemistry .
108 Debromination of acidified aerosol increases reactive bromine by 30%, although global models may
109 underestimate Arctic reactive bromine when considering only open ocean-sourced SSA (Schmidt et al.,
110 2016). Initial literature on Arctic reactive bromine chemistry identified aerosol particles as a potential
111 saline surface for reactive bromine photochemistry (Fan and Jacob, 1992; Vogt et al., 1996) and field
112 studies confirmed that SSA is depleted in bromide (Ayers et al., 1999; Hara et al., 2018). If one supposes
113 that SSA can only be produced from the open ocean source of SSA, the lack of Arctic Ocean open water
114 during the winter/spring is at odds with observations of high SSA concentrations observed during the
115 winter months in polar regions (Wagenbach et al., 1998; Huang et al., 2018). The formation of SSA from
116 the sublimation of blowing snow particles over the Arctic Ocean was proposed as an alternate SSA
117 production mechanism (Yang et al., 2008, 2010, 2019). Recent field studies have confirmed the direct
118 production of SSA from blowing snow (Frey et al., 2020). A blowing snow SSA mechanism was
119 implemented in the global chemical model GEOS-Chem and was able to explain wintertime SSA
120 enhancements over the Arctic (Huang and Jaeglé, 2017) as well as CALIOP-detected aerosol particle
121 abundance (Huang et al., 2018) and high levels of Arctic BrO detected by satellites in spring (Huang et
122 al., 2020).

123 Snowpack containing bromide salts was also identified as a source of reactive bromine (Tang and
124 McConnell, 1996). Molecular bromine was measured above the snowpack at levels up to 25 pmol/mol
125 (Foster et al., 2001). Field experiments demonstrate that the snowpack emits Br₂, Cl₂, and BrCl, with
126 emission affected by ambient ozone levels, the snowpack ratio of bromide to chloride, and exposure to
127 sunlight (Pratt et al., 2013; Custard et al., 2017). Box modeling found that the flux of reactive bromine
128 from the surface of the Arctic Ocean sea ice is a prerequisite for bromine activation (Lehrer et al., 2004).
129 Box modeling found that both HOBr and BrNO₃ can be converted to Br₂ in the snowpack (Wang and

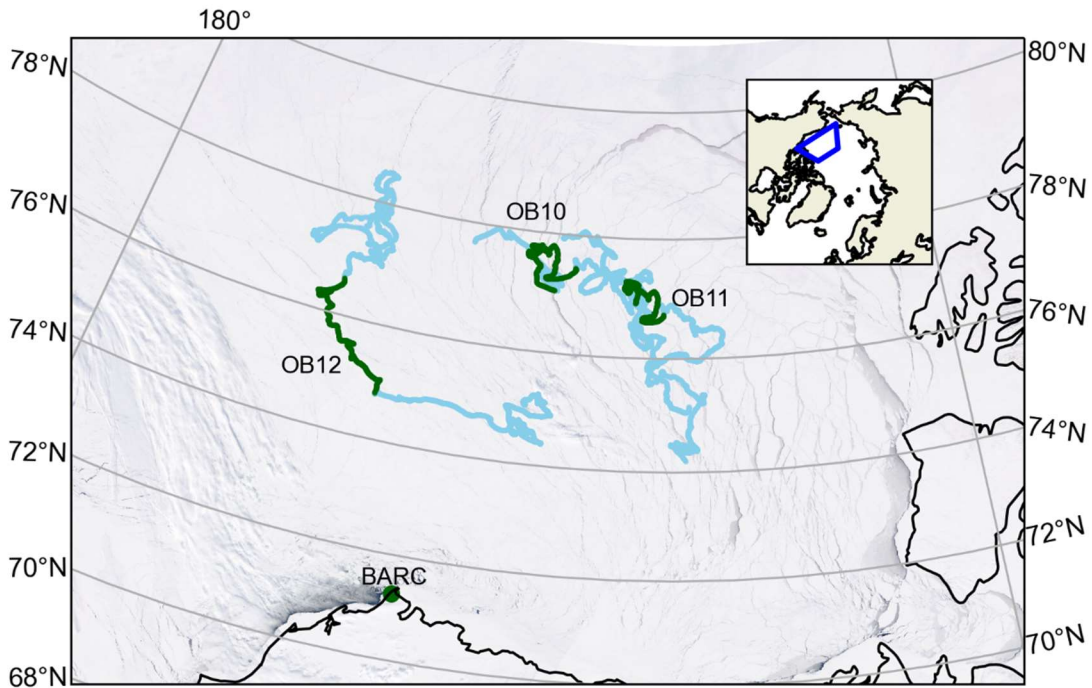
130 Pratt, 2017). Detailed one dimensional models of the snowpack-air interface find that reactive bromine
131 production can occur in the interstitial air between snowpack grains (Thomas et al., 2011; Toyota et al.,
132 2014), with ozone depletion events arising from snowpack reactive bromine production (Thomas et al.,
133 2011; Toyota et al., 2014; Cao et al., 2016). However, a detailed snowpack model coupled to an
134 atmospheric model would be sensitive to important parameters such as snowpack bromide content and
135 acidity of the air-ice interface that are highly variable across the Arctic (Toom-Sauntry and Barrie, 2002;
136 Krnavek et al., 2012). A mechanism to parameterize the release of molecular bromine from snowpack
137 upon deposition of ozone, HOBr, and BrNO₃ was implemented in the GEM-AQ model and captured
138 many of the observed features of reactive bromine in the Arctic troposphere (Toyota et al., 2011). The
139 mechanisms from Toyota et al. (2011) assumes a 100% yield of molecular bromine on deposition of
140 HOBr or BrNO₃ (see Figure 1 PACK) and a diurnally varying yield of Br₂ on ozone deposition of 7.5%
141 during the daytime (solar elevation angle > 5°) and 0.1% during the nighttime (solar elevation angle < 5°)
142 (see Figure 1 PACK). In the Toyota et al. (2011) parameterization, the daytime yield of Br₂ from ozone
143 was increased to 7.5% to match surface ozone depletion observations and is based on the assumption that
144 photochemical reactions in the snowpack would trigger a bromine explosion and amplify the net release
145 of Br₂ (Toyota et al., 2011). Herrmann et al (2021) implemented the Toyota et al. (2011) mechanism in
146 WRF-Chem and found snowpack Br₂ production was capable of replicating ozone depletion events
147 observed in multiple datasets. Marelle et al. (2021) implemented a surface snowpack mechanism based on
148 Toyota et al. (2011) and a blowing snow SSA mechanism based on Yang et al. (2008) and Huang and
149 Jaeglé (2017) and found improved prediction of ozone depletion events, the majority of which were
150 triggered by the snowpack mechanism. The Toyota et al. (2011) mechanism was also implemented in the
151 EMAC model and replicated many of the features of reactive bromine events observed by satellite-based
152 GOME sensor (Falk and Sinnhuber, 2018).

153 Field campaigns have directly observed the production of SSA from blowing snow (Frey et al.,
154 2020) as well as production of Br₂ from the snowpack (Pratt et al., 2013) in the environment. This
155 manuscript uses both production mechanisms for the first time in the global chemical model GEOS-
156 Chem. We devised a set of six model runs to test each mechanism individually and together as well as one
157 control run using neither mechanism. We compare BrO simulated in each model run against extensive
158 ground-based observations of BrO made from February to June 2015. This set of modeling scenarios
159 allows identification of the effects of each mechanism on BrO as well as the synergistic effects of both
160 mechanisms working together.

161 2. Data sources and methods

162 2.1 MAX-DOAS observation platforms

163 Multiple axis differential optical absorption spectroscopy (MAX-DOAS) remotely measures the
164 vertical profile of BrO (Hönninger and Platt, 2002; Carlson et al., 2010; Frieß et al., 2011; Peterson et al.,
165 2015; Simpson et al., 2017). BrO is commonly used as a proxy for total tropospheric reactive bromine
166 (Chance, 1998; Richter et al., 1998; Wagner and Platt, 1998; Theys et al., 2011; Choi et al., 2012). MAX-
167 DOAS instruments were mounted on all of the fifteen floating autonomous platforms (O-Buoys) deployed
168 in the Arctic sea ice as a part of the National Science Foundation-funded Arctic Observing Network
169 project (Knepp et al., 2010). Since MAX-DOAS requires sunlight to operate, measurements are not
170 available in winter. Spring observations on the O-Buoys typically begin in April when there is enough O-
171 Buoy solar power to defrost the MAX-DOAS viewport. Figure 2 shows the O-Buoys active during 2015.
172 O-Buoy 10 was deployed into sea ice in fall 2013 and measured reactive halogen chemistry in spring
173 2014 and 2015. Most O-Buoys were destroyed in the summer, crushed between fragments of melting sea
174 ice. However, O-Buoy 10 survived summer 2014 in an intact ice floe, survived the winter of 2014-15,
175 and re-started MAX-DOAS observations in April 2015. O-Buoys 11 and 12 were deployed in fall 2014
176 and also re-started observing BrO in April 2015. Figure 2 shows the GPS-derived tracks of the O-Buoys
177 for their full deployment and highlights the O-Buoy locations from April to June 2015 when the BrO
178 observations considered in this analysis were gathered. A MAX-DOAS instrument of the same design
179 was deployed at the Barrow Arctic Research Center (BARC) on the coast of the Arctic Ocean located at
180 156.6679°W, 71.3249°N near Utqiagvik, AK (Simpson, 2018), also shown in Figure 2. Unlike the O-
181 Buoy MAX-DOAS systems, which were powered by batteries and solar panels, the BARC MAX-DOAS
182 was powered from local utilities and was able to defrost its viewport to gather BrO observations earlier in
183 the year, including February and March 2015. The BARC MAX-DOAS data was compared with two O-
184 Buoy style MAX-DOAS instruments deployed on Icelander platforms (deployed on top of sea ice instead
185 of within) and measurements from the various MAX-DOAS systems were found to be comparable
186 (Simpson et al., 2017). The reactive bromine season ends when the BrO slant column densities fall below
187 the instrument detection limit and do not recover, which we call the seasonal end date (Burd et al., 2017).
188 All O-Buoy and BARC (Utqiagvik) data are available at arcticdata.io (Simpson et al., 2009) (Simpson,
189 2018). More information on the time periods of spring BrO observations can be found in Swanson et al.
190 (2020) and Burd et al. (2017). For comparison to the MAX-DOAS BrO observations, GEOS-Chem model
191 simulations are sampled along the GPS-derived paths of O-Buoys 10, 11 and 12 as well as at BARC.



192

193 **Figure 2: Locations of MAX-DOAS BrO observations used in this work.**

194 Blue lines show the drift tracks of O-Buoys, with green showing the locations with valid BrO
 195 measurements in spring 2015. Location of Barrow Arctic Research Center (BARC) in Utqiagvik indicated
 196 by green dot. True color MODIS imagery on 1 April 2015 shows typical sea ice coverage (NASA 2015).
 197 Inset map shows location of map grid within northern hemisphere.

198 **2.2 MAX-DOAS profile retrieval**

199 Vertical profiles of BrO were derived from MAX-DOAS observations by means of optimal
200 estimation inversion procedures detailed in Peterson et al. (2015) with settings detailed in Simpson et al.
201 (2017). The HeiPro optimal estimation algorithm (Frieß et al., 2006, 2019) is used to retrieve a vertical
202 profiles of BrO between the surface and 4km from the MAX-DOAS observations. Examination of the
203 averaging kernels from each MAX-DOAS retrieval finds the retrieved vertical profile of BrO is best
204 represented by two quantities: the vertical column density of BrO in the lowest 200 m, and the vertical
205 column density of BrO in the lowest 2000 m of the troposphere referred to in this manuscript as BrO_{LTcol}
206 (Peterson et al., 2015). It was shown in Peterson et al. (2015) that these two quantities were largely
207 independent of each other, were fairly insensitive to variations in the assumed prior profile, and
208 represented the ~2-3 degrees of freedom for signal indicated by the optimal estimation retrieval. An
209 important consideration of this method is that when the visibility is poor, the MAX-DOAS is unable to
210 traverse the lowest 2000m AGL and the BrO_{LTcol} cannot be measured accurately. Therefore, our quality-
211 control algorithm eliminates BrO_{LTcol} observations when the degrees of freedom for signal in the lofted
212 (200m - 2000m AGL) layer were below 0.5 (Simpson et al., 2017). The average fitting error (1 σ error) of
213 BrO_{LTcol} during spring 2015 was 5.6×10^{12} molecules/cm².

214 **2.3 SSA production from open ocean**

215 Seafoam from breaking waves and bursting of bubbles forms aerosol droplets suspended in the
216 marine boundary layer (Lewis and Schwartz, 2004). We calculate emission of sea salt aerosol particles
217 from the open ocean as a function of wind speed and sea surface temperature (SST) using the mechanism
218 initially described in Jaeglé et al. (2011) and updated with decreased emissions over cold (SST < 5°C)
219 ocean waters (Huang and Jaeglé, 2017). Two separate SSA tracers are transported: accumulation mode
220 SSA ($r_{\text{dry}} = 0.01\text{--}0.5 \mu\text{m}$) and coarse mode SSA ($r_{\text{dry}} = 0.5\text{--}8 \mu\text{m}$). Sea salt bromide is emitted assuming
221 bromine content of 2.11×10^{-3} kg Br per kg of dry SSA (primarily NaCl) based on the mean ionic
222 composition of sea water (Sander et al., 2003). Bromide content is tracked separately on accumulation
223 mode SSA and on coarse mode SSA. Freshly emitted SSA is alkaline and can be titrated to a pH of 5 by
224 uptake of acid gases SO₂, H₂SO₄, and HNO₃ (Alexander et al., 2005). Heterogeneous chemical reactions
225 can convert SSA-transported bromide into gaseous reactive bromine species in the atmosphere. We run
226 our open ocean SSA calculations at 0.5° latitude x 0.625° longitude spatial resolution using the
227 harmonized emissions component (HEMCO) for highest possible detail (Keller et al., 2014; Lin et al.,
228 2021) including cold water corrections used in Jaeglé et al. (2011). Production of SSA from open oceans
229 followed by advection can lead to reactive bromine recycling over Arctic Ocean sea ice. Each of our
230 model runs reads the dataset generated offline by HEMCO rather than spend computational time

231 replicating open ocean SSA emissions. We call our control run using only open ocean SSA emissions
232 BASE.

233 **2.4 Blowing snow SSA production**

234 Snow can be lofted from the snowpack into the lowest layers of the troposphere by high wind
235 speeds, where it can undergo saltation (bouncing leading to fragmentation) and sublimation to form SSA
236 (Yang et al., 2008, 2010; Frey et al., 2020). This process is modeled as a function of humidity, ambient
237 temperature, wind speed, and the salinity of the blowing snow (Yang et al., 2008, 2010). We assume that
238 snowpack exists on all sea ice surfaces during the Arctic Spring after snow accumulation during winter on
239 sea ice of all ages. Three thresholds must be met for SSA production from blowing snow (Dery and Yau,
240 1999; Déry and Yau, 2001). A temperature threshold restricts SSA production from blowing snow to
241 temperatures below freezing. The humidity threshold is based on relative humidity with respect to ice.
242 Sublimation from snow crystals cannot occur if the air is saturated, and no SSA is produced if RH_{ice} is
243 greater than 100%. The wind speed threshold requires 10-m wind speed to be greater than a threshold
244 value defined in Equation 1 for any production of SSA (Dery and Yau, 1999; Déry and Yau, 2001).

$$245 \quad U_t = 6.975 + 0.0033(T_s + 27.27)^2 \quad (1)$$

246 The wind speed threshold (U_t) is dependent on surface temperature (T_s) in Celsius with a minimum
247 threshold of 6.975 m/s at -27.27 °C and a maximum threshold at 0 °C of 9.429 m/s. The 10-m wind speed
248 threshold is the most stringent and often controls the production of SSA from blowing snow.

249 Production of blowing snow SSA is highly sensitive to surface wind speed. We use the highest
250 resolution surface wind speed dataset to ensure the most accurate modeling of SSA and reactive bromine.
251 The MERRA-2 Global Reanalysis Product has a 0.5° latitude x 0.625° longitude resolution which is
252 typically re-gridded to a lower resolution for global chemical modeling. Previous use of the snowpack
253 blowing snow SSA mechanism used MERRA-2 data re-gridded to either 2° x 2.5° or 4° x 5° latitude and
254 longitude (Huang and Jaeglé, 2017; Huang et al., 2018, 2020). Re-gridding to coarser spatial resolution
255 may smooth out the highest 10-m wind speeds by averaging them with lower wind speeds in the grid cell.
256 The Utqiagvik MERRA-2 10-m wind speeds at different spatial resolutions are shown in Supplemental
257 Figures S1, S2 and S3 to illustrate this effect. Average Utqiagvik 10-m wind speeds for 2015 are 5.3 m/s
258 at 2° x 2.5° resolution and 5.5 m/s at 0.5° x 0.625° resolution. The maximum Utqiagvik 10-m wind speed at
259 MERRA-2 2° x 2.5° is 16.3 m/s, while the maximum wind speed at MERRA-2 0.5° x 0.625° is 19.3 m/s.
260 These extremely high wind speed events are more common at higher spatial resolution and can contribute
261 an outsized amount of SSA to the marine boundary layer. Supplemental Figure S4 shows the measured
262 10-m wind speed at BARC, along with daily average threshold wind speed (Equation 1). Spikes in daily

263 averaged wind speed at BARC in April can contribute to SSA formation and justify the use of high-
264 resolution MERRA-2 wind speed data.

265 Snow salinity is influenced by snow age and the material underlying the snow (Krnavek et al.,
266 2012). The median surface snowpack salinity near Utqiagvik was measured at 0.67 practical salinity units
267 (PSU)PSU for 2-3 weeks old sea ice, 0.12 PSU for thicker first year ice, and 0.01 PSU for multi-year ice
268 (MYI) (Krnavek et al., 2012). Snow salinity is also a function of snow depth above sea ice, with blowing
269 surface snow having much lower salinity than snow at depth that is in contact with the sea ice (Frey et al.,
270 2020). Domine et al. (2004) measured median salinity at 0.1 PSU on snowpack over first year ice and
271 0.02 PSU on snowpack over multi-year ice. In this analysis we use a salinity of 0.1 PSU on first-year sea
272 ice as in Huang et al. (2020). The production of reactive bromine from sea ice types is entirely dependent
273 on PSU in this parameterization. Previous modeling efforts have used 0.01 PSU for MYI (Huang et al.,
274 2018) and underestimate BrO production in high Arctic areas with increased MYI coverage. The bromide
275 content of surface snow over MYI is enriched by deposition of SSA and trace gases, and MYI regions
276 may play a role in springtime halogen chemistry (Peterson et al., 2019). Previous analysis of O-Buoy data
277 found no statistically significant differences in springtime BrO between regions of the Arctic (Swanson et
278 al., 2020). We use 0.05 PSU for snowpack on MYI as in Huang et al. (2020).

279 Another important parameter for SSA formation is the number of SSA particles formed from each
280 blowing snowflake. A value of 5 particles per snowflake was used in Huang and Jaeglé (2017) based on
281 wintertime observations of supermicron and sub-micron SSA at Barrow. Values of 1 and 20 particles per
282 snowflake have been tested (Yang et al., 2019) but it is unclear which value was more realistic. We use a
283 particle formation value of 5 particles per snow grain as in Huang et al. (2020).

284 Snowpack may be enriched or depleted in bromide compared to seawater, which is thought to be
285 an effect of atmospheric deposition or release of bromine from snowpack (Krnavek et al., 2012).
286 Snowpack enrichment due to atmospheric deposition is less pronounced when snowpack salinity is high,
287 with snowpack containing $1000 \mu\text{M Na}^+$ (approximately 0.06 PSU) or more never exceeding twice the
288 seawater ratio of bromine to chloride (Krnavek et al., 2012). Domine et al. (2004) found an increased
289 enrichment factor of five times seawater in snow with a salinity of $100 \mu\text{M Cl}^-$ (approximately 0.006
290 PSU). We use a snowpack enrichment factor of bromide five times that of seawater as in Huang et al.
291 (2020) where this enrichment best agreed with GOME-2 observations. However, we note that a bromide
292 enrichment factors five times seawater exceeds enrichment factors of two measured in snowpack with a
293 salinity of 0.1 PSU (Krnavek et al., 2012).

294 Our choice of model input settings is similar to Huang et al. (2020) but we will be running the
295 blowing snow SSA mechanism in HEMCO at a 0.5° latitude x 0.625° longitude spatial resolution. The
296 model run using the results of our high-resolution blowing snow SSA HEMCO simulation is called
297 BLOW.

298 **2.5 Snowpack emissions of molecular bromine**

299 We base our Br₂ emissions scheme on Toyota et al. (2011) and Marelle et al. (2021), which
300 prescribe a yield of Br₂ upon snowpack deposition of ozone, BrNO₃ and HOBr. In other modeling studies,
301 this simplified deposition-based mechanism captured the synoptic-scale behavior of reactive bromine
302 production across the Arctic (Toyota et al., 2011; Falk and Sinnhuber, 2018; Herrmann et al., 2021;
303 Marelle et al., 2021). These modeling studies used different yields of Br₂ upon deposition over land
304 snowpack, multi-year ice, and first year ice, restricting the production of molecular bromine from ozone
305 deposition to first year ice surfaces. None of these studies were coupled to a snowpack model tracking
306 snow bromide, and effectively assume an infinite bromide reservoir with Br₂ production limited only by
307 the deposition flux and Br₂ yield.

308 Field studies indicate that snowpack over multi-year ice, first-year ice, and land regions may
309 contribute to reactive bromine chemistry. Krnavek et al. (2012) found snow bromide content spanning six
310 orders of magnitude, with individual samples taken from multi-year ice, first-year ice, and land regions
311 showing variability of up to three orders of magnitude for each region. Analysis of variance in
312 tropospheric BrO from 2011-2016 found no statistically significant differences in tropospheric BrO
313 between different regions of the Arctic (Swanson et al., 2020). Both coastal snowpack and multi-year ice
314 regions may produce reactive bromine. Molecular bromine production has been observed from coastal
315 snowpack on exposure to ozone (Pratt et al., 2013; Custard et al., 2017). Airborne sampling has observed
316 enhanced BrO up to 200 km inland (Peterson et al., 2018). Snow above multi-year sea ice regions is
317 depleted in bromide, indicating that it may play a role in Arctic bromine chemistry (Peterson et al., 2019).

318 Our modeling study tests the hypothesis that all snow has a uniform ability to produce molecular
319 bromine, effectively assuming an infinite bromide reservoir with Br₂ production limited only by the
320 deposition flux. We differ from previous model parameterizations in allowing uniform Br₂ production
321 upon snowpack deposition of ozone, BrNO₃ and HOBr over all sea ice surfaces and selected coastal
322 snowpack regions. We expect higher predictions of snowpack molecular bromine production than recent
323 modeling efforts (Herrmann et al., 2021; Marelle et al., 2021) in which ozone deposition over land and
324 multi-year ice surfaces did not produce molecular bromine.

325 **2.5.1 Snowpack Br₂ production over sea ice**

326 We assume a uniform production of Br₂ on deposition to snowpack over oceanic ice whether the
327 ice is first-year sea or multi-year sea ice. We use MERRA-2 fractional ocean ice coverage fields, which
328 introduces some artifacts. MERRA-2 classifies the freshwater Great Lakes as ocean, but sea ice and
329 snowpack on those frozen lakes is unlikely to have sufficient bromide to support large Br₂ fluxes due to
330 its distance from the ocean. Therefore, we specifically prohibit snowpack Br₂ emissions in the Great
331 Lakes region (between 41° N and 49° N latitude and 75° W and 93° W longitude). This choice is in
332 agreement with McNamara et al. (2020), who found road salt derived aerosol particles are responsible for
333 80-100% of atmospheric ClNO₂ in Michigan with no strong indication for a source of reactive halogens
334 from nearby Great Lakes.

335 **2.5.2 Snowpack Br₂ production over land**

336 We wish to only enable production of Br₂ over land if the snowpack is sufficiently enriched in
337 bromide. Snowpack over land surfaces and glaciers may be enriched in bromide by oceanic SSA sources
338 (Jacobi et al., 2012, 2019). The distance that SSA may be transported inland from the coast is limited by
339 geographical features such as mountains. Based on direct observations of reactive bromine chemistry up
340 to 200 km from the Alaskan coastline (Peterson et al., 2018), we include unlimited production of Br₂ from
341 specific land grid cells within 200 km of the coast upon deposition of ozone, HOBr, and BrNO₃. We only
342 allow the fraction of each grid cell that is within 200 km of the coastline (Group and Stumpf, 2021) to
343 produce molecular bromine. We further restrict snowpack Br₂ emissions to locations that are less than 500
344 m above sea level, because higher elevation locations are unlikely to be enriched by sea spray. This
345 altitude screen eliminates Br₂ emissions from coastal mountains such as the Alaskan Rockies, the Brooks
346 Range in Alaska, and the Scandinavian Mountains as well as from the Greenland Plateau. Halogen
347 chemistry may occur over the Greenland ice sheet (Stutz et al., 2011) contrary to this screen, but this will
348 have minimal impact on the regions of interest in this manuscript.

349 Our final screen is based on the average snow depth in each land grid cell. Both modeling studies
350 (Thomas et al., 2011; Toyota et al., 2014) and field studies (Domine et al., 2004; Pratt et al., 2013;
351 Custard et al., 2017; Frey et al., 2020) agree that bromine chemistry can occur in the better ventilated and
352 illuminated top of the snowpack. Regions with less than 10 cm of snowpack may not have sufficient
353 snow for reactive bromine chemistry, thus we only produce snowpack Br₂ when the average snow depth
354 in a land grid cell is 10 cm or greater. This screen prevents molecular bromine production in the lower
355 latitude regions with minimal snow coverage and is necessary because ozone deposition to plants in
356 snow-free grid cells often exceeds the slow deposition of ozone to snowpack and would not be expected
357 to produce Br₂.

358 **2.5.3 Diurnal yield of Br₂ on ozone deposition**

359 We choose two alternate assumptions for the yield of Br₂ during the day. Toyota et al. (2011)
 360 initially assumed a constant yield of Br₂ from ozone deposition of 0.1% based on laboratory observations
 361 of nighttime bromine activation on ozone deposition (Oum et al., 1998; Wren et al., 2010, 2013) and then
 362 adjusted the daytime yield of Br₂ on ozone deposition to 7.5% to better match surface ozone mixing ratios
 363 measured at coastal stations. This increased daytime yield value was chosen based on the assumption that
 364 photochemistry may trigger an autocatalytic cycle leading to a 75-fold increase in Br₂ yield. The
 365 PHOTOPACK runs uses the increased daytime Br₂ yield of 7.5% when the solar elevation angle is 5° or
 366 greater. Previous implementations of the snowpack mechanism (Toyota et al., 2011; Herrmann et al.,
 367 2021; Marelle et al., 2021) predict ozone deposition velocities over Arctic sea ice on the order of 0.01
 368 cm/s. Our model predicts similar ozone deposition rates over polar open ocean of 0.009 cm/s (Pound et
 369 al., 2020), but our model currently predicts the deposition velocity of ozone over Arctic sea ice between
 370 0.02 cm/s and 0.1 cm/s based on the month (see Supplemental Figure S5), with higher values influenced
 371 by proximity to the coast as described in Bariteau et al. (2010). Thus, our PHOTOPACK run may predict
 372 much higher Br emissions than previous snowpack predictions despite the same yield values due to
 373 differences in deposition. To match out magnitude of Br₂ production with previous implementations of
 374 the snowpack mechanism (Toyota et al., 2011; Herrmann et al., 2021; Marelle et al., 2021) we add two
 375 PACK runs with a constant Br₂ yield on ozone deposition of 0.1% based on yield values in Toyota et al.
 376 (2011). Both PACK and PHOTOPACK runs assume 100% conversion of deposited HOBr and BrNO₃ to
 377 Br₂. Table 1 shows further model run yield details.

378 **Table 1 Model run settings**

379 Sea salt aerosol particles are produced from blowing snow as detailed in Section 2.5. Daytime is defined
 380 as when the solar elevation angle is greater than 5°, nighttime is defined as when the solar elevation angle
 381 is less than 5°.

Model Run	Blowing snow SSA produced	Millimoles Br yielded per mole O3 deposited (daytime)	Millimoles Br yielded per mole O3 deposited (nighttime)
BASE	FALSE	0	0
BLOW	TRUE	0	0
PACK	FALSE	1	1
BLOW+PACK	TRUE	1	1
PHOTOPACK	FALSE	75	1
BLOW+PHOTOPACK	TRUE	75	1

382

383 2.6 GEOS-Chem chemistry and transport model

384 The GEOS-Chem global atmospheric chemistry and transport model (Bey et al., 2001) simulates
385 emissions, transport, and chemistry of atmospheric trace gases and aerosols, including halogens. The
386 chemical mechanism in GEOS-Chem 12.9.3 (<http://www.geos-chem.org>, last access 29 October 2019,
387 DOI:10.5281/zenodo.3974569) includes HO_x-NO_x-VOC-O₃-halogen-aerosol tropospheric chemistry
388 (Mao et al., 2013; Fischer et al., 2014; Fisher et al., 2016; Travis et al., 2016; Wang et al., 2021). The
389 model has been regularly and consistently updated to reflect current understanding of heterogeneous and
390 gas-phase halogen chemistry.

391 Halogens in the troposphere may be sourced from photooxidation of halocarbons, emissions of
392 iodine from the ocean surface, downward transport of halogens from the stratosphere, and release of
393 halogens through heterogeneous chemistry on SSA. Figure 1 shows a simplified version of the GEOS-
394 Chem reaction scheme focusing on tropospheric bromine reactions and reservoirs. Heterogeneous
395 reactions for release of reactive bromine from aerosol surfaces were added to GEOS-Chem (Parrella et
396 al., 2012) and have been updated to include multiphase reactions involving cloud aerosols and inter-
397 halogen reactions between bromine, chlorine and iodine species (Schmidt et al., 2016; Sherwen et al.,
398 2016a; Wang et al., 2019b) as well as input from the stratosphere (Eastham et al., 2014). Recent updates
399 also include reactions between sulfur (IV) species and HOBr, which lead to a 50% decrease in Br_y due to
400 the scavenging of HOBr on aerosol surfaces containing sulfur (Chen et al., 2017). These HOBr-sulfur(IV)
401 reactions are critical in moderating tropospheric BrO in the mid latitudes (Zhu et al., 2019). In GEOS-
402 Chem 12.9 the halogen chemical mechanism was modified extensively to include chlorine chemistry as
403 detailed in Wang et al. (2019b) with updated halogen-sulfur (IV) rates (Liu et al., 2021), reaction of S(IV)
404 + HOCl, and improved cloud pH calculation from Shah et al. (2020). For the simulations here, GEOS-
405 Chem uses the Modern-Era Retrospective Analysis for Research and Applications, version 2 (MERRA-2)
406 assimilated meteorological fields (Gelaro et al., 2017) re-gridded from native resolution of 0.5°x0.625°
407 latitude and longitude to 2°x2.5° using a reduced vertical grid of 47 layers.

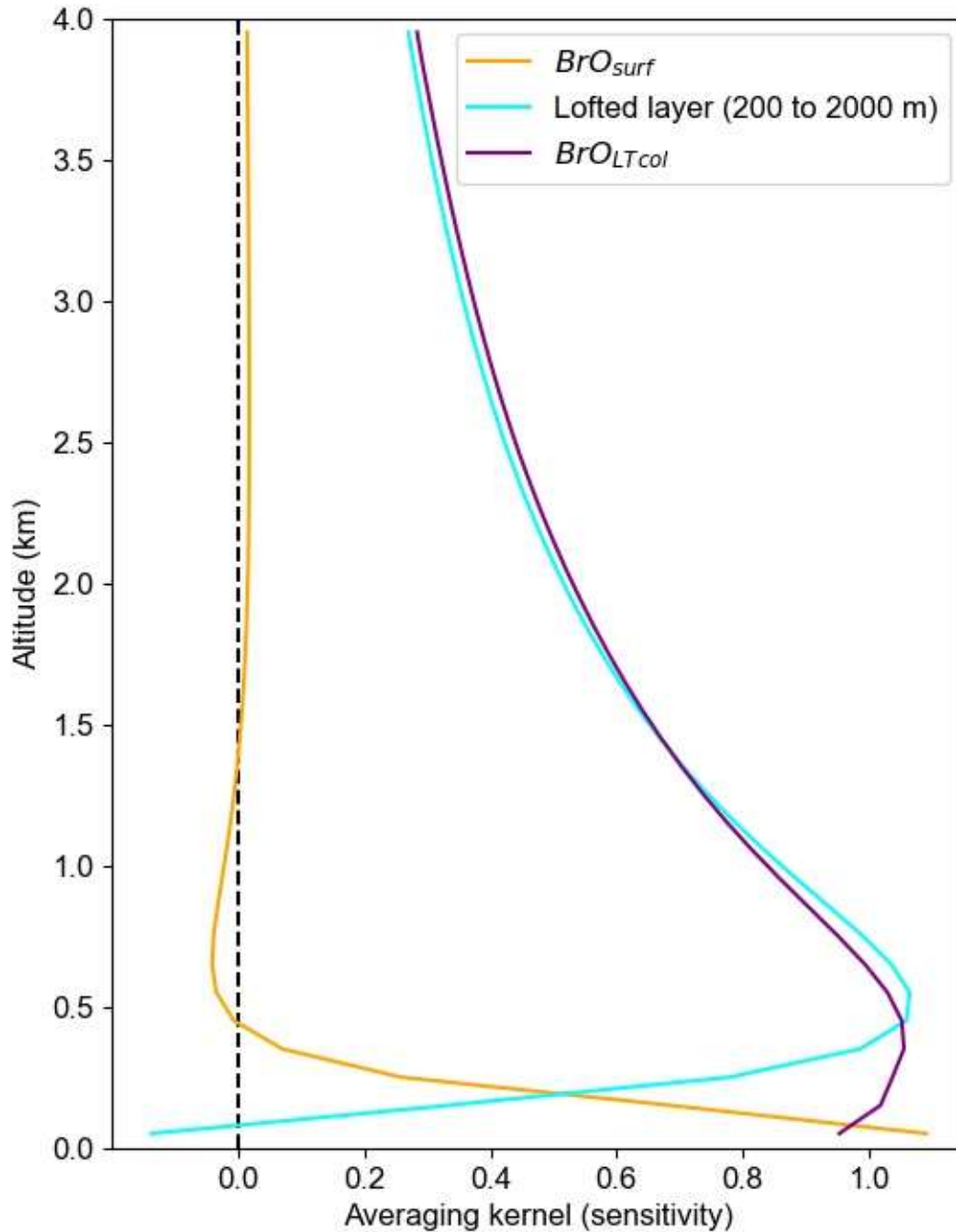
408 We initialize our model in October 2014 from a full-chemistry benchmark file, allowing for 6
409 months of spin up before our period of interest spanning from March to November 2015. We run six
410 different model simulations with settings detailed in Table 1. The base model (BASE) includes the
411 halogen sources described above but no Arctic-specific halogen sources. The BLOW simulation adds
412 SSA production from blowing snow following Huang et al (2020) but using a more recent version of
413 GEOS-Chem. The PACK simulation adds snowpack Br₂ emissions using a constant yield from O₃
414 deposition. The PHOTOPACK simulation also emits Br₂ from snowpack but increases the Br₂ yield from

415 O₃ deposition under sunlight. These blowing snow SSA and snowpack sources are combined in the
416 BLOW+PACK and BLOW+PHOTOPACK simulations.

417 **2.7 Comparing GEOS-Chem results to MAX-DOAS vertical column densities**

418 GEOS-Chem simulates BrO mixing ratios for each of its 47 atmospheric layers. Reducing the
419 vertical resolution of the more-resolved GEOS-Chem predictions to be comparable to the coarser MAX-
420 DOAS data is necessary for appropriate comparison (Rodgers and Connor, 2003). To compare the
421 GEOS-Chem profiles with these two grid-coarsened quantities, we grid-coarsen the averaging kernels
422 produced by the HeiPro retrieval algorithm using Supplemental Equation S1 from Payne et al. (2009) to
423 the partial column averaging kernels shown in Figure 3. We use the average of all April averaging kernels
424 that pass our quality criteria (>0.5 DOFS in the lofted layer), which generally represents non-cloudy
425 conditions. We calculate modeled BrO_{LTcol} by applying the partial column averaging kernels shown in
426 Figure 3 to the GEOS-Chem modeled vertical BrO profiles.

427 Figure 3 shows the average partial column averaging kernel for the surface layer (0-200m AGL)
428 has near unit sensitivity to BrO at the ground, decaying to about 0.5 at 200m AGL then to zero at about
429 400m AGL, as desired. The sensitivity of the BrO_{LTcol} is near unity from about the surface to 600m AGL,
430 then slowly decays with 0.5 sensitivity at 2000m AGL. The resulting sensitivity to mid-tropospheric BrO
431 means that free-tropospheric BrO produced by the GEOS-Chem model contributes to modeled BrO_{LTcol},
432 albeit at 50% or lower sensitivity, even if the GEOS-Chem-predicted free-tropospheric BrO is above the
433 nominal 2000m top of the integration window. The residual sensitivity of the BrO_{LTcol} averaging kernel
434 above 2000m is caused by the limited ability of ground-based MAX-DOAS to distinguish the true altitude
435 of BrO at non-tangent geometries (higher viewing elevation angles) that are required to view BrO at these
436 higher altitudes. Figure 3 shows that BrO above 4 km makes only a small contribution to the modeled
437 BrO_{LTcol}, which was not included in the BrO_{LTcol}.



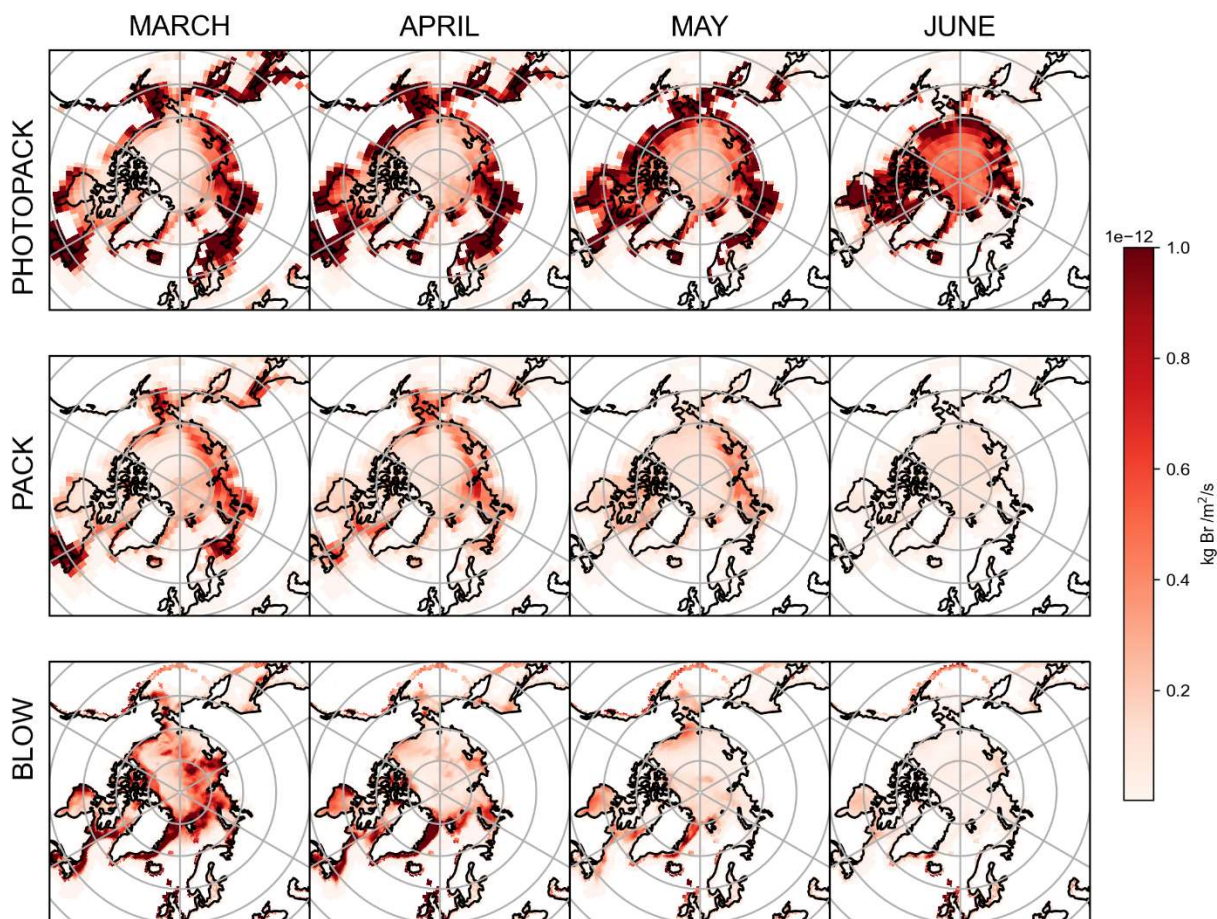
438

439 **Figure 3: Averaging kernels showing the sensitivity of retrieved $\text{BrO}_{\text{LTcol}}$ and retrieved BrO_{surf} to**
 440 **BrO at a range of altitudes.**

441 Each line represents a row of the averaging kernel matrix. BrO_{surf} is the column from the surface to 200 m
 442 and $\text{BrO}_{\text{LTcol}}$ is the column up to 2000 m.

443 Although it has been suggested in the literature (von Clarmann and Glatthor, 2019) that averaged
 444 averaging kernels can cause problems, we do not report data when there are clouds and thus are only
 445 using the more consistent averaging kernels that occur under clear sky conditions. We use other criteria
 446 related to vertical visibility to identify clear skies. As described in Peterson et al. (2015), the information
 447 content (DOFS) in the lofted layer is nearly linearly related to the aerosol optical depth. We find that the

448 slant column density of the O₂-O₂ collisional dimer (aka O₄) observed at 20° elevation angle is correlated
 449 with the lofted DOFS (Supplemental Figure S6). From this correlation we find that observations of clear
 450 sky conditions have 20° elevation angle O₄ dSCD > 10⁴³ molecule²cm⁻⁵ and use this cut to distinguish
 451 clear sky versus clouds. To assure that GEOS-Chem results are only compared to the clear-sky
 452 observational data, we apply this clear sky screen to the measured BrO_{LTcol} timeseries. The use of this
 453 screen also assists in minimizing variability in the averaging kernels and thus allowing the April averaged
 454 partial column averaging kernels (Figure 3) to be applied for clear skies at any time of the year.



455
 456 **Figure 4: Mean snowpack Br₂ emissions and p-Br⁻ by month, as simulated by GEOS-Chem.**
 457 The top row shows emissions of Br₂ in the PHOTOPACK run, the middle row shows the emissions of
 458 Br₂ in the PACK run, and the bottom row shows emissions of p-Br⁻ from adding the BLOW mechanism.
 459 **3. Examining reactive bromine in the Arctic spring**
 460 **3.1 Snowpack Br₂ emissions**
 461 The top two rows of Figure 4 shows PHOTOPACK and PACK average snowpack Br₂ emissions
 462 for each spring month. The emission of Br₂ in PHOTOPACK increases over the Arctic Ocean in May and

463 June, when the sun is above the horizon for up to 24 hours per day and ozone deposition yield is almost
464 always at the photo-enhanced level of 7.5%. Notably, Br₂ emissions over the Arctic Ocean in the
465 PHOTOPACK and BLOW+PHOTOPACK runs are highest in June when the sun is nearly always five
466 degrees above the horizon and surface temperatures may drop below freezing. The PACK emissions are
467 lower than the PHOTOPACK Br₂ emissions by an order of magnitude and shows a seasonal cycle with a
468 high BrO_{LTcol} in April and May with a decrease in May and June. While our ozone deposition velocities
469 (see Supplemental Figure S5) over Arctic sea ice are much higher than previous estimates of an
470 approximate magnitude of 0.01 cm/s (Toyota et al., 2011), the PHOTOPACK run highlights that a 75-
471 fold increase in daytime Br₂ yield can lead to predictions of increased Br₂ production over the North Pole
472 in June. Monthly satellite observations show that BrO reaches a minimum over the Arctic Ocean in June
473 (Richter et al., 1998).

474 Coastal land regions within 200 km of the coastline have some of the highest modeled snowpack
475 Br₂ emissions (see Figure 4 rows 1 and 2). Within GEOS-Chem, deposition rates are greatest over land,
476 less rapid over ice-covered ocean, and lowest over open ocean (see Supplemental Figure S5). Lower dry
477 deposition velocities over the ice-covered Arctic Ocean lead to decreased deposition and conversion to
478 Br₂. In GEOS-Chem, ozone mixing ratios and deposition are over three orders of magnitude larger than
479 BrNO₃ and HOBr mixing ratios and deposition over the Arctic Ocean, and ozone deposition contributes
480 more than half of total Br₂ emitted in the PACK and BLOW+PACK runs. Our snowpack mechanism
481 assumes that all ozone deposited to the surface of a grid cell reacts with the snowpack cover and produces
482 Br₂. This assumption is more appropriate in the barren snow-covered coastal tundra but may be less
483 accurate in areas where deposition to vegetation dominates. This nonconservative approach may lead to
484 overestimation of Br₂ emissions from snowy vegetated surfaces. Our screens for snowpack emissions
485 described in section 1.3.5 tried to minimize these effects but may not work perfectly due to finite grid cell
486 resolution and other challenges. Increased Br₂ emissions observed in Figure 4 in northern Europe may
487 also be partially driven by increased local mixing ratios of ozone and NO_x over industrialized regions
488 such as the Kola Peninsula.

489 **3.2 Blowing snow aerosol bromide emissions**

490 The bottom row of Figure 4 shows the total quantity of particulate bromide released by the
491 blowing snow SSA mechanism in the BLOW runs. Emissions over the Arctic Ocean decline each month
492 after the March maximum as rising temperatures increase the wind speed threshold for blowing snow
493 SSA production. Some icy coastal regions with frequently high wind speeds such as the Aleutian Islands
494 south of Alaska and the eastern coast of Greenland continue to emit SSA p-Br⁻ in April, and the extremely
495 high winds in the Aleutians enable SSA production into May. The location of specific high-wind storm

496 systems in spring 2015 may be evident in the darker red spots over the Arctic Ocean, which are
 497 particularly noticeable over the Eurasian and Central Arctic in March. These monthly averages are only
 498 accurate for the months in spring 2015 and may not be spatially representative of blowing snow SSA
 499 production in other years.

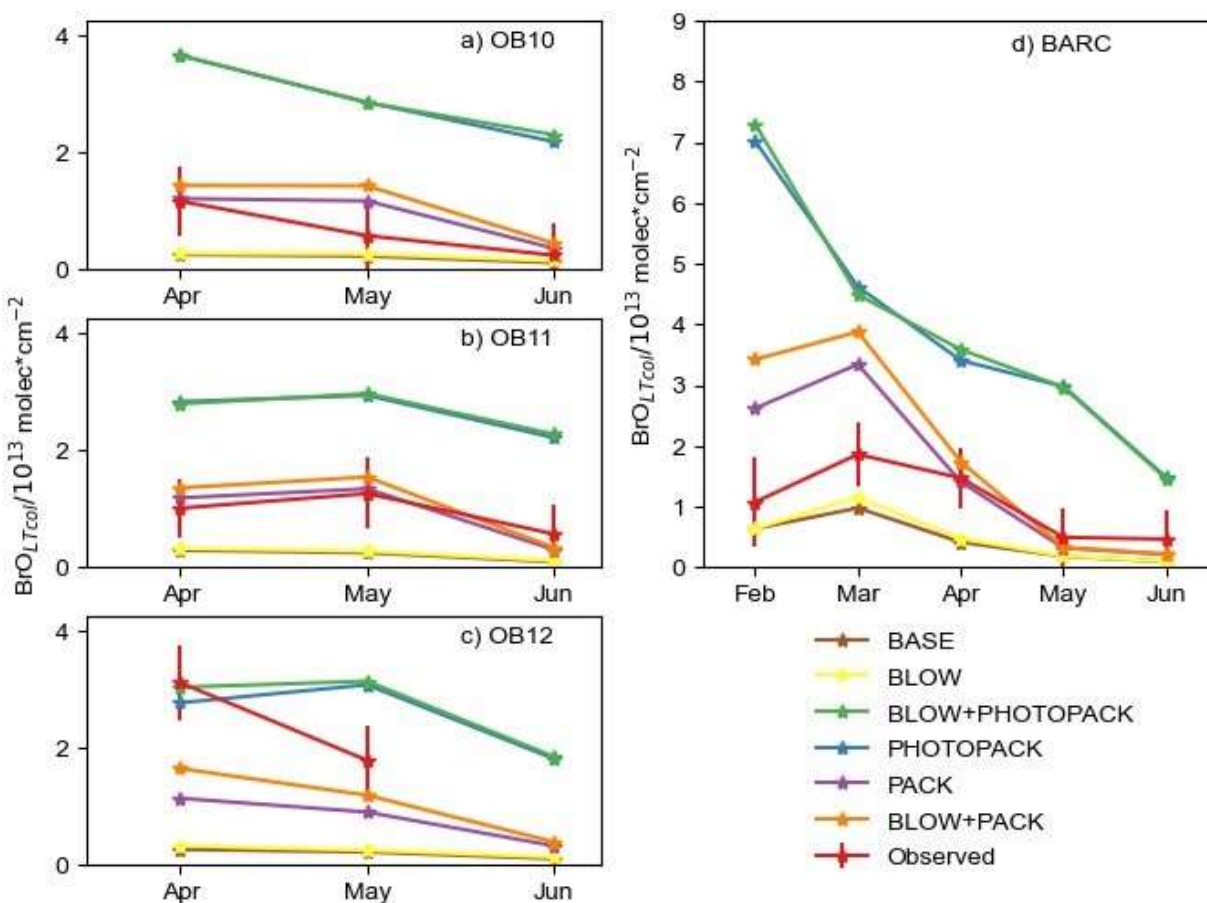
500 The impact of the blowing snow SSA emissions on measured BrO is minimal on O-Buoys in the
 501 Beaufort Gyre, possibly due to the spatial and seasonal variations in SSA p-Br⁻ emissions. Figure 4 shows
 502 that 2015 SSA production was highest in March and April on the Eurasian and Central sector of the
 503 Arctic, and thus the O-Buoys deployed as shown in Figure 2 are less exposed to the effects of SSA
 504 production than the Arctic as a whole. Particulate bromide must be activated from SSA by heterogeneous
 505 reactions as in Figure 1 and Table 3, leading to photochemical cycles that sustain further activation of
 506 bromide from SSA. The dearth of sunlight over the Arctic Ocean in early March coincides with the
 507 greatest SSA p-Br⁻ production and means that the increased February SSA p-Br⁻ emissions may not lead to
 508 a direct increase in BrO.

509 **Table 2: Model root mean square error by run and location.**

510 Root mean squared model error (RMSE) shown in BrO_{LTcol}/10¹² molec/cm² RMSE calculated as the
 511 square root of the mean of the squared errors for all times with valid observed BrO_{LTcol} in Spring 2015.

Units in BrO _{LTcol} /10 ¹² molec/cm ²	OB10	OB11	OB12	Utqiagvik
BASE	9.9	12.9	22.9	13.0
BLOW	9.7	12.7	22.4	12.5
PACK	9.9	10.0	18.6	15.2
BLOW+PACK	10.1	10.1	15.7	17.5
PHOTOPACK	30.0	24.8	26.2	30.1
BLOW+PHOTOPACK	30.3	24.6	26.3	31.4

512



514

515 **Figure 5: Monthly average BrO_{LTcol} in observations and model**

516 Monthly averages of BrO at a) O-Buoy 10, b) O-Buoy 11, c) O-Buoy 12, and d) BARC at Utqiaġvik only
 517 using predictions and observations when dSCDO₄ > 1*10⁴³ molecules²cm⁻⁵. Observations with average 1σ
 518 error shown in red. All units in 10¹³ molecules/cm².

519

520 **3.3 Snowpack Br₂ emissions have more impact than blowing snow SSA on monthly BrO abundance**

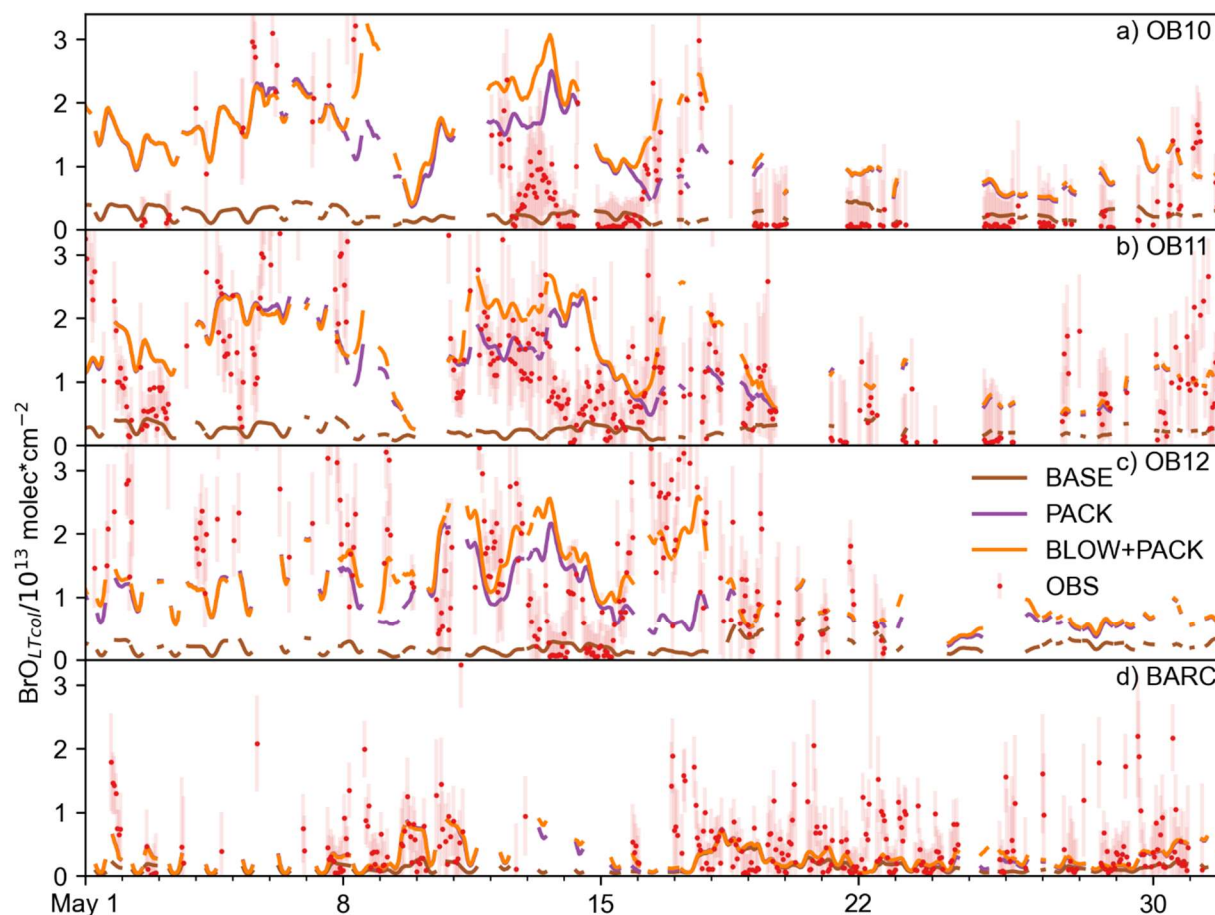
521 Increased levels of bromine have been historically seen at Utqiaġvik during February, March,
 522 April and May (Berg et al., 1983). Previous O-Buoy data analysis noted BrO dropping to zero in June
 523 (Burd et al., 2017). Figure 5 shows monthly averaged modeled BrO_{LTcol} at Utqiaġvik and on the O-Buoys
 524 for each model configuration. The difference in GEOS-Chem modeled monthly averaged BrO_{LTcol} for O-
 525 Buoys is minimal between the BASE and BLOW runs, the PHOTOPACK and BLOW+PHOTOPACK
 526 runs, and the PACK and BLOW+PACK runs. Both BASE and BLOW runs predict near-zero BrO_{LTcol} on
 527 all O-Buoys and during most months at Utqiaġvik. The exception to this is the slight increases in monthly
 528 modeled BrO_{LTcol} to 1*10¹³ molecules/cm² in March and April. This BASE increase in BrO_{LTcol} indicates
 529 that oceanic SSA rather than blowing snow SSA can affect modeled BrO at Utqiaġvik due to its closer

530 proximity to open ocean regions than the O-Buoys. The increases in BrO from the BASE model due to
531 the addition of BLOW, most evident at Utqiagvik in March 2015, are a result of increased particulate
532 bromide available for activation on aerosol surfaces. The PACK and BLOW+PACK runs show the
533 highest skill in reproducing observations, falling within the monthly average of hourly measured $\text{BrO}_{\text{LTcol}}$
534 error for 9 of the 13 months plotted in Figure 5. Both PACK and BLOW+PACK replicate the observed
535 monthly pattern on O-Buoy 11 and at Utqiagvik especially well. The seasonal pattern of maximum
536 modeled $\text{BrO}_{\text{LTcol}}$ at Utqiagvik in March followed by a decrease to near-zero modeled $\text{BrO}_{\text{LTcol}}$ in May is
537 replicated in both runs despite the overprediction of $\text{BrO}_{\text{LTcol}}$ in February and March. The BLOW+PACK
538 monthly $\text{BrO}_{\text{LTcol}}$ is between 1×10^{12} molecules/cm² and 1×10^{13} molecules/cm² higher than PACK monthly
539 $\text{BrO}_{\text{LTcol}}$ due to the addition of blowing snow SSA. This increase is most pronounced in February and
540 March at Utqiagvik when lower temperatures lead to lower threshold wind speeds and increased SSA
541 production (see Supplemental Figure S4).

542 The inclusion of increased daytime yield of snowpack Br_2 drives monthly average $\text{BrO}_{\text{LTcol}}$ above
543 3×10^{13} molecules/cm² in the PHOTOPACK and BLOW+PHOTOPACK runs from February until June,
544 far above peak observed monthly $\text{BrO}_{\text{LTcol}}$ of 2×10^{13} molecules/cm². The PHOTOPACK and
545 BLOW+PHOTOPACK runs show steady decline in $\text{BrO}_{\text{LTcol}}$ from February to June at Utqiagvik.
546 Predictions of PHOTOPACK and BLOW+PHOTOPACK monthly June $\text{BrO}_{\text{LTcol}}$ above 2×10^{13}
547 molecules/cm² on the O-Buoys is due to increasing photo-assisted local snowpack Br_2 emissions over the
548 Arctic Ocean (see Figure 5). The PHOTOPACK mechanism predicts monthly average $\text{BrO}_{\text{LTcol}}$ within
549 observational error only on O-Buoy 12 in April. Aside from this replication of the sparsely sampled O-
550 Buoy 12 April $\text{BrO}_{\text{LTcol}}$, the PHOTOPACK mechanism overestimates $\text{BrO}_{\text{LTcol}}$.

551 Table 2 shows the root mean squared error (RMSE) of each model run as compared to $\text{BrO}_{\text{LTcol}}$
552 observations in at each different location in Spring 2015. The PACK and BLOW+PACK runs have the
553 lowest RMSE on O-Buoys 11 and 12, and among the lowest RMSE on O-Buoy 10. Utqiagvik shows the
554 lowest RMSE of 1.25×10^{13} molec/cm² for the BLOW run, although the PACK run is not too far off at
555 1.57×10^{13} molec/cm². Despite the fact that BLOW+PACK has a higher RMSE of 1.75×10^{13} molec/cm² at
556 Utqiagvik, the BLOW+PACK run performs the best or near the best of all runs on the O-Buoys and
557 includes both known processes for Arctic reactive bromine production. The PHOTOPACK and
558 BLOW+PHOTOPACK runs with increased daytime yield have a consistently high RMSE of 2.46×10^{13}
559 molec/cm² or higher, often double the RMSE of other model runs.

560



562

563 **Figure 6: May Hourly BrO_{LTcol} timeseries**

564 Hourly timeseries of BLOW+PACK, PACK, and BASE BrO_{LTcol} on a) O-Buoy 10, b) O-Buoy 11, c) O-
 565 Buoy 12 and d) BARC at Utqiagvik in the 2015 Arctic Spring. Observations and error bars in red, BASE
 566 BrO_{LTcol} in brown, PACK BrO_{LTcol} in purple, and BLOW+PACK BrO_{LTcol} in orange. All BrO_{LTcol} plotted
 567 continuously except for gaps where dSCDO₄ > 1*10⁴³ molecules²cm⁻⁵.

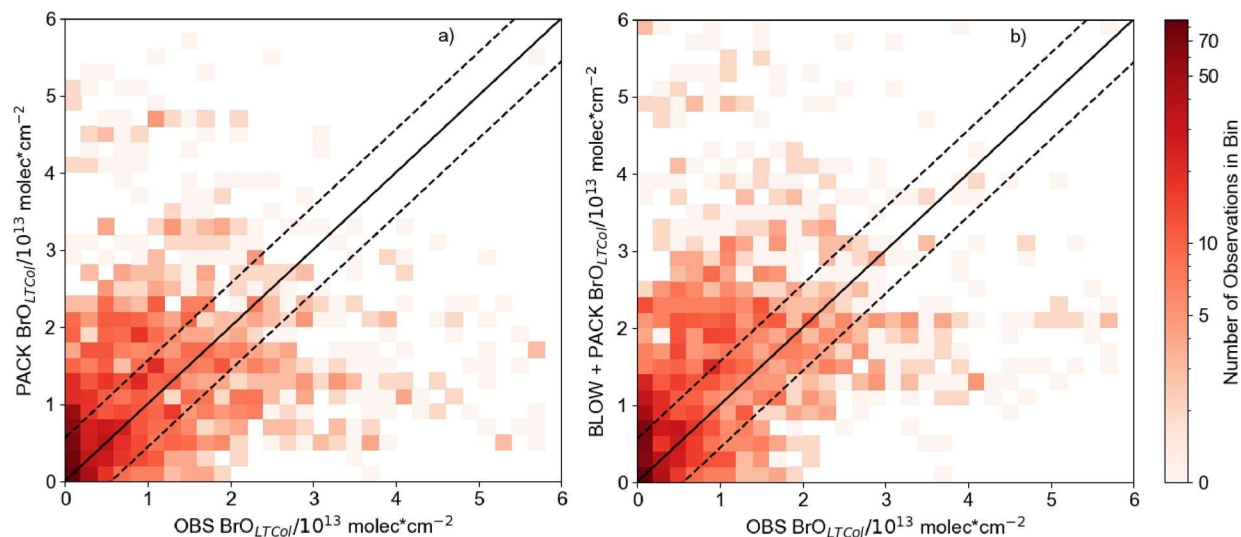
568 **3.4 BLOW+PACK run best replicates hourly BrO events in mid and late May**

569 The model's hourly predictions of BrO_{LTcol} in May 2015 are shown in Figure 6 for the BASE,
 570 PACK, and BLOW+PACK runs. Figure 6 screens modeled BrO_{LTcol} for times when dSCD O₄ > 1*10⁴³
 571 molecules²cm⁻⁵, while Supplemental Figures S7 and S8 make only direct comparisons between
 572 observations of BrO_{LTcol} on the O-Buoys (S7) and at Utqiagvik (S8) throughout all of Spring 2015. The
 573 O-Buoys show fluctuations in observed BrO_{LTcol} during May and show consistent increased columns of
 574 BrO_{LTcol} from May 10 to May 20. The BASE run never rises above 10¹³ molecules/cm² and underpredicts
 575 most May hourly BrO_{LTcol}, although BASE predicts monthly BrO_{LTcol} on OB10 for May and June. Both
 576 PACK and BLOW+PACK runs show better skill in replicating BrO_{LTcol}. The addition of the snowpack
 577 mechanism allows us to predict increased BrO_{LTcol} in late May on O-Buoys 10 and 11. This points to the
 578 role of surface snowpack in late-season events in agreement with the findings of Burd et al. (2017).

579 We can identify the role of blowing snow SSA by comparing the PACK and BLOW+PACK runs.
580 Both PACK and BLOW+PACK runs underestimate $\text{BrO}_{\text{LTcol}}$ during the first ten days of May. BrO
581 predictions and show higher variability and peaks starting on May 10. The blowing snow SSA
582 mechanism increases BLOW+PACK $\text{BrO}_{\text{LTcol}}$ on May 12 and 13. PACK is skilled at replicating observed
583 O-Buoy 11 $\text{BrO}_{\text{LTcol}}$ on both days, and both PACK and BLOW+PACK are within observational $\text{BrO}_{\text{LTcol}}$
584 error on May 13.

585 A BrO event also occurs on May 13 on O-Buoy 10. While the strength of the O-Buoy 10 BrO
586 event is overestimated by PACK and BLOW+PACK, the shape of that event is reproduced in both runs.
587 Observed $\text{BrO}_{\text{LTcol}}$ decreases rapidly on all O-Buoys after May 14, and the model is unable to track this
588 sharp decrease. Rapid changes in $\text{BrO}_{\text{LTcol}}$ may be caused by sharp edges in BrO-enriched airmasses such
589 as those seen by Simpson et al. (2017). GEOS-Chem run at this resolution cannot replicate abrupt
590 changes in BrO, but it does slowly decrease $\text{BrO}_{\text{LTcol}}$ to reach $\text{BrO}_{\text{LTcol}}$ to less than 10^{13} molecules/cm² on
591 May 16. The BLOW+PACK mechanism is skilled in replicating the magnitude and features of a mid-
592 May BrO event on O-Buoys 10 and 11.

593 Figure 7 shows all Spring 2015 $\text{BrO}_{\text{LTcol}}$ observations on O-Buoys 10, 11, 12, and BARC plotted
594 against PACK $\text{BrO}_{\text{LTcol}}$ and BLOW+PACK $\text{BrO}_{\text{LTcol}}$. The increase in $\text{BrO}_{\text{LTcol}}$ on adding BLOW leads to
595 fewer underpredictions of observations (see bottom right section of Figure 7b). The Pearson correlation
596 coefficient (r) between PACK $\text{BrO}_{\text{LTcol}}$ and observed $\text{BrO}_{\text{LTcol}}$ is 0.33, improving to 0.39 on addition of
597 BLOW in the BLOW+PACK run. Other runs show less skill in replicating observations, with a BASE
598 $\text{BrO}_{\text{LTcol}}$ Pearson correlation to observations of 0.19 and a BLOW $\text{BrO}_{\text{LTcol}}$ Pearson correlation to
599 observations of 0.23. We also performed a simple linear regression to determine the relationship between
600 predictions and observations for each run. The slope of the line of best fit improves drastically on addition
601 of PACK, changing from 0.06 for BASE and 0.07 for BLOW to 0.33 for PACK and 0.44 for
602 BLOW+PACK. There is a positive synergistic effect on the slope of the line of best fit when using both
603 BLOW and PACK in combination rather than individually. The use of both BLOW and PACK
604 mechanisms implements literature findings on the processes influencing Arctic reactive bromine and
605 increases correlation between GEOS-Chem predictions and observations.



606

607 **Figure 7: Hourly modeled $\text{BrO}_{\text{LTcol}}$ versus $\text{BrO}_{\text{LTcol}}$ observations**

608 Two dimensional histograms showing density of GEOS-Chem predicted $\text{BrO}_{\text{LTcol}}$ s versus all observed
 609 Spring 2015 hourly Br_{LTcol} , with a) PACK $\text{BrO}_{\text{LTcol}}$ shown at left sorted into square bins of 0.2 with an
 610 Pearson r correlation to observations of 0.33 and b) BLOW+PACK $\text{BrO}_{\text{LTcol}}$ on the bottom sorted into
 611 square bins of 0.2 with Pearson r correlation to observations to 0.39. All units are in molecules/ cm^2 . 1:1
 612 line drawn in the center in black, with a margin of the average observational error plotted in dashed black
 613 lines around the central 1:1 line.

614 **4. Arctic Spring reactive bromine modeling discussion**

615 **4.1 Use of both mechanisms in conjunction leads to best prediction of tropospheric BrO results**

616 Initial implementation of this snowpack mechanism in Toyota et al. (2011) increased the daytime
 617 yield of Br_2 from ozone deposition to 7.5% to improve agreement between observed and modeled surface
 618 ozone mixing ratios. Toyota et al. (2011) also increased the surface resistance of ozone to 10^4 s/m,
 619 decreased deposition velocities on Arctic snowpack to approximately 0.01 cm/s. Our model using a
 620 constant yield of Br from ozone deposition performs best, despite observations that sunlight has an effect
 621 on reactive bromine recycling in the snowpack (Pratt et al., 2013; Custard et al., 2017). GEOS-Chem does
 622 not explicitly model heterogeneous photochemistry within the snowpack interstitial space but does
 623 include heterogeneous bromine chemistry on aerosol particle surfaces after the Br_2 is emitted from the
 624 snowpack into the lowest model layer. The updates to GEOS-Chem halogen chemistry (Schmidt et al.,
 625 2016; Sherwen et al., 2016b; Chen et al., 2017; Wang et al., 2019b) should be mechanistically sufficient
 626 to model daytime heterogeneous chemistry of reactive bromine on aerosol surfaces. We note that
 627 improvements to GEOS-Chem have increased the explicit modeling of these photochemical recycling and
 628 amplification processes, possibly reducing the need for empirical increases to daytime yields.

629 Our findings differ from recent implementations of the snowpack mechanism in Herrmann et al.
 630 (2021) and Marelle et al. (2021). While all snowpack mechanisms are based on Toyota et al. (2011),
 631 several large differences in model configuration and mechanism implementation explain these

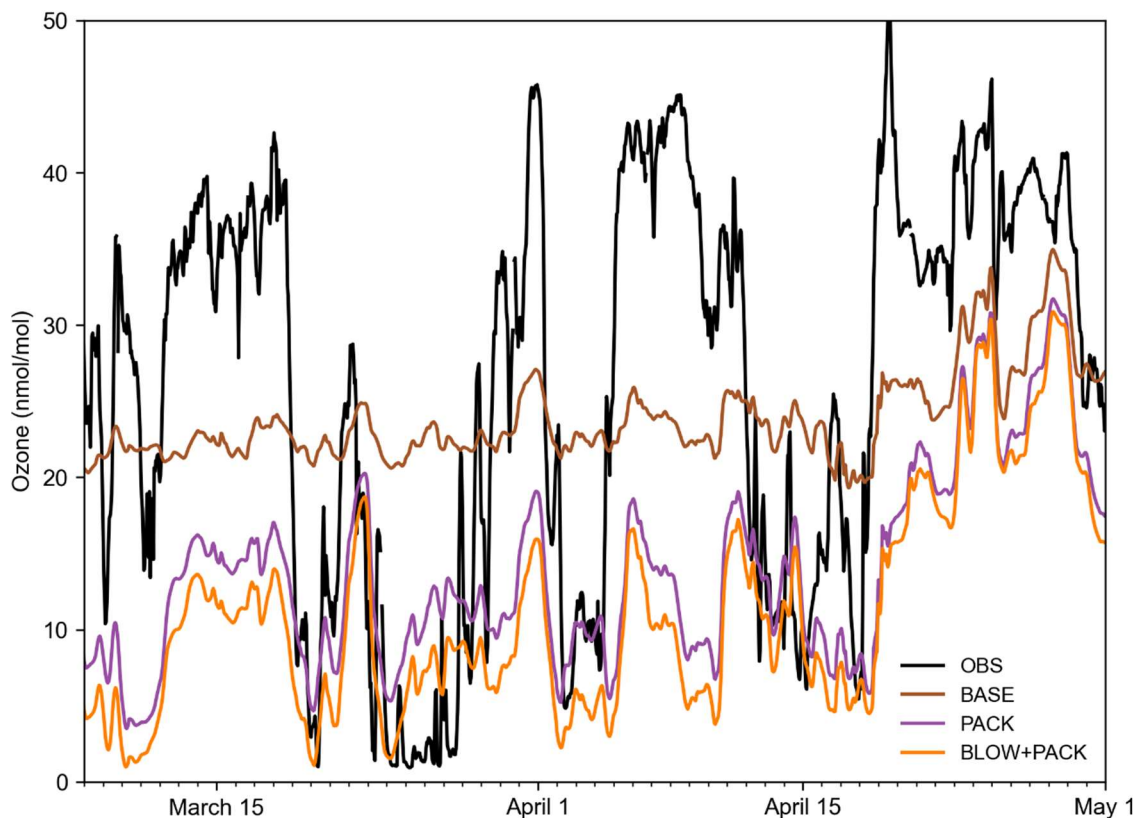
632 differences. We allow Br₂ production from ozone deposition over all snow surfaces, leading to much
633 higher Br₂ production over MYI and coastal regions. Land snowpack can produce Br₂ on exposure to
634 ozone and sunlight (Pratt et al., 2013; Custard et al., 2017) and Figure 4 shows our coastal snowpack
635 producing large quantities of Br₂. Tropospheric reactive bromine chemistry has been observed up to 200
636 km inland from the coast (Peterson et al., 2018). Marelle et al. (2021) underestimates BrO in late March
637 and overestimates Utqiaġvik BrO in early April. This seasonal pattern may be due to increased daytime
638 ozone yield on first year ice near Utqiaġvik in April. Herrmann et al. (2021) found that HOBr and BrNO₃
639 deposition was more important in driving snowpack Br₂ production and that the daytime yield of 7.5%
640 Br₂ on ozone deposition underpredicted BrO. We find that ozone contributes slightly more than HOBr
641 and BrNO₃ because we allow for Br₂ production on ozone deposition over multi-year ice and coastal
642 snowpack regions. The temporal scale of this manuscript spans the entire year, while Herrmann et al.
643 (2021) only spans February, March, and April. Our longer timescale highlights the issue of increased
644 daytime Br₂ yield during May and June (see Figure 4 PHOTOPACK) with increased emissions over the
645 Arctic Ocean that are not in agreement with satellite observations of minimal Arctic tropospheric BrO in
646 June (Richter et al., 1998).

647 **4.2 Addition of PACK mechanism increases surface ozone predictive skill**

648 The Barrow Arctic Research Center (BARC) in Utqiaġvik has the most comprehensive coverage
649 of surface ozone in Spring 2015. A constant yield of 0.1% Br₂ from ozone deposition allows us to
650 approximate the average vertical extent of ozone depletion events at Utqiaġvik in May 2015. The increase
651 in Br_y in the PACK and BLOW+PACK runs is confined to the lowest 1000 m of the atmosphere (see
652 Supplemental Figure S9). Ozone depletions, caused by reactive bromine chemistry, often only occur
653 within the lowest 1000 m of the troposphere (Bottenheim et al., 2002; Salawitch et al., 2010). Previous
654 studies have found evidence of lofted BrO in plumes at altitudes up to 900 m AGL (Peterson et al., 2017).
655 The monthly average Utqiaġvik May surface ozone in BLOW and BLOW+PACK is 22 nmol/mol,
656 matching mean May surface ozone from 1999-2008 (Oltmans et al., 2012). The PHOTOPACK runs
657 generate mean May surface ozone depletion to approximately 5 nmol/mol, far below the May mean. The
658 PACK and BLOW+PACK runs duplicate the approximate vertical extent of elevated bromine levels and
659 the strength of typical May ozone depletion.

660 Figure 8 shows hourly ozone predictions alongside BARC ozone observations (McClure-Begley,
661 Petropavlovskikh, and Oltmans, 2014). The BASE model fails to replicate variance in ozone measured at
662 BARC in Utqiaġvik, with a Pearson correlation coefficient to observations of 0.35. Adding PACK
663 improves Pearson correlation to 0.47, within rounding error of BLOW+PACK Pearson correlation of
664 0.47. Both PACK and BLOW+PACK significantly improve model performance in replicating ozone

665 depletions in such as the depletion below 30 nmol/mol from March 20 to March 29 but fail to track the
666 subsequent recovery of ozone to background levels on April 1. Predicted PACK ozone does not recover
667 to background levels up to the height of roughly 1000 m. A similar pattern where our model replicates
668 low ozone but fails to predict the recovery of ozone to background levels occurs on April 5 and 15.
669 Examination of ozone profiles in GEOS-Chem found that GEOS-Chem underpredicts tropospheric ozone
670 by 10-20 ppb north of 60° latitude (Wang et al., 2021), which contributes to the low ozone predictions in
671 our runs. Previous modeling of Utqiagvik spring 2012 ozone in WRF-Chem found a similar linear
672 correlation coefficient of 0.5 to BROMEX observations (Simpson et al., 2017) when using both blowing
673 snow and snowpack mechanisms (Marelle et al., 2021). We are biased low compared to observations,
674 with a root mean square error of 17.0 nmol/mol in BLOW+PACK compared to a root mean square error
675 of 12.9 nmol/mol in Marelle et al. (2021). This may be partially due to limited vertical resolution in
676 GEOS-Chem that may be inadequate to describe shallow surface-based temperature inversions and
677 subsequent recovery. The high bias in ozone deposition velocity over sea ice surfaces may also contribute
678 to low ozone mixing ratios near the surface.



680

681 **Figure 8: Hourly Utqiagvik ozone timeseries**

682 Hourly timeseries of BLOW+PACK, PACK, and BASE ozone at Utqiagvik in the 2015 Arctic Spring.
 683 Ozone observations at BARC in black (McClure-Begley, Petropavlovskikh and Oltmans, 2014), BASE
 684 ozone in brown, PACK ozone in purple, and BLOW+PACK ozone in orange. Gaps indicate missing
 685 observational data.

686

687 A similar improvement in ozone predictions on the addition of PACK is seen on the O-Buoys, but
 688 is harder to quantify due to observational gaps in ozone data. Supplemental Figure S10 shows hourly
 689 ozone predictions graphed over O-Buoy 11 observations and Supplemental Figure S11 shows hourly
 690 ozone predictions graphed over O-Buoy 12. O-Buoy 10 was not able to gather an observations of ozone in
 691 2015. The clearest impact of PACK in Figures S10 and S11 is seen in early April, with observed ozone
 692 dropping near zero nmol/mol and PACK and BLOW+PACK runs dropping to five nmol/mol while the
 693 BASE run remains near 20 nmol/mol. Figure S10 shows that ozone predictions on O-Buoy 10 in May are
 694 less accurate, failing to fall below 10 nmol/mol ozone while observations show ozone dropping near the
 695 detection limit. The O-Buoys appear to experience more late-season ozone depletion events that GEOS-
 696 Chem fails to replicate, possibly due to warming temperatures increasing vertical mixing and replenishing
 697 ozone near the surface.

698

699 **Table 3: Arctic Tropospheric Reactions Rates by Model Run**
700 Rates for each of the reactions listed in Figure 1 organized by GEOS-Chem run. All units are listed as
701 millions of moles per hour across the region shown in Supplemental Figure S14. R in equation R2 refers
702 to any organic molecule. Y in equation 1 represents NO, Cl, or H. X in equation HR6a represents either
703 Br or Cl. PHOTOPACK and BLOW+PHOTOPACK are excluded as they severely overpredict BrO as
704 seen in Figures 4 and 5.

	BASE	BLOW	PACK	BLOW+PACK	Reaction Equation
R1	17.57	17.77	27.7	28.4	BrO + YO -> Br+ O ₂
R2	236.28	261.75	435.74	472.14	Br + O ₃ -> BrO + O ₂
R3	0.7	0.84	1.38	1.54	Br + RH -> HBr, Br + HO ₂ -> HBr
R4	0.01	0.01	0.02	0.02	HBr + OH -> Br + H ₂ O
R5	9.41	9.47	14.41	14.01	BrO + HO ₂ -> HOBr
R6	1.63	2.4	12.78	16.16	BrO + BrO -> Br ₂ + O ₂
R7	0.03	0.06	0.04	0.06	BrO + ClO -> BrCl + O ₂
R8	2.8	2.94	5.69	5.86	BrO + NO ₂ -> BrNO ₃
R9	0	0	0	0	Br ₂ + OH -> Br + HOBr
R10	0.15	0.17	1.39	1.64	Br + BrNO ₃ -> Br ₂ + NO ₃
R11	0.18	0.18	0.55	0.7	Br + NO ₂ -> BrNO ₂
HR1a	0.04	0.03	0.15	0.1	HOBr + HBr -> Br ₂ + H ₂ O
HR1b	0.79	0.95	1.47	1.68	HOBr + p-Br ⁻ -> Br ₂ + OH ⁻
HR2	0.17	0.21	0.38	0.38	HOBr+H ₂ O+HSO ₃ ⁻ -> H ₂ SO ₄ +HBr+OH ⁻
HR3	0.25	0.29	0.43	0.44	BrNO ₃ + H ₂ O -> HNO ₃ + HOBr
HR4a	0	0	0	0	HBr + O ₃ -> HOBr + O ₂
HR4b	0.07	0.09	0.14	0.15	p-Br ⁻ +O ₃ +H ₂ O-> HOBr+O ₂ +OH ⁻
HR5	0	0	0	0	BrNO ₃ + HCl -> BrCl + HNO ₃
HR6a	0	0	0	0	HOX + HX-> BrCl+H ₂ O
HR6b	0.29	0.54	0.37	0.68	HOBr + p-Cl ⁻ -> BrCl + OH ⁻
HR7a	0	0	0	0	HBr + ClNO _x -> BrCl + HNO _x
HR7b	0	0	0	0	p-Br ⁻ +ClNO _x +H ₂ O-> BrCl+HNO _x +OH ⁻
HR8	0	0	0	0	p-Br ⁻ + IO _x > IBr + O _x
P1	1.38	1.76	6.04	7.24	Br ₂ +hv-> 2Br
P2	203.54	227.07	362.89	392.04	BrO + hv -> Br + O
P3	8.45	8.11	12.6	11.75	HOBr +hv-> OH+Br
P4	0.36	0.37	0.57	0.56	BrNO ₃ +hv-> BrO + NO ₂
P5	2.04	2.1	3.24	3.17	BrNO ₃ +hv-> Br + NO ₃
P6	0.18	0.18	0.55	0.7	BrNO ₂ +hv-> Br+NO ₂
P7	0.35	0.63	0.45	0.76	BrCl +hv-> Br +Cl
P8	0	0	0	0	BrI +hv-> Br +I

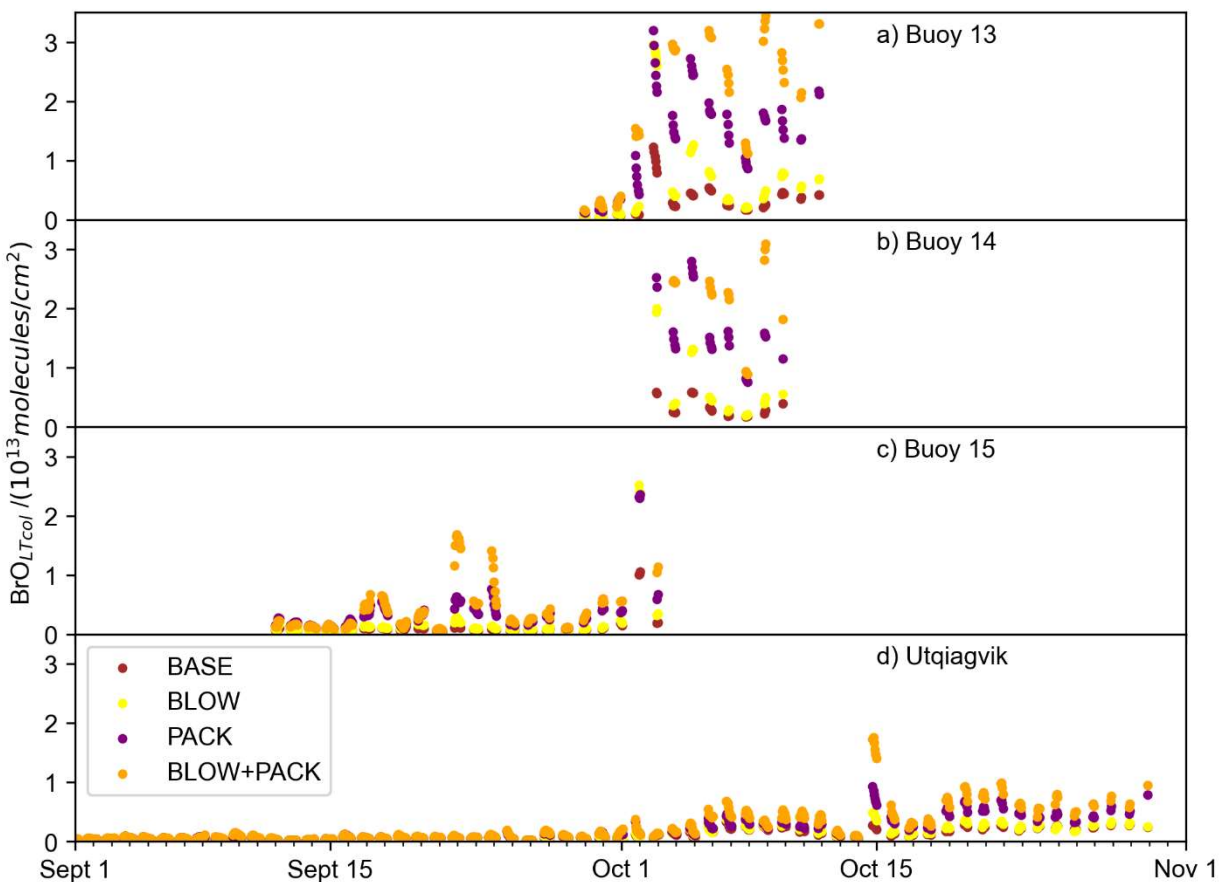
705

706 **5. Examining reactive bromine in the Arctic in September and October**

707 O-Buoys deployed during fall 2015 measured BrO slant column densities characterized by noise
708 around zero (see Supplemental Figures S12 and S13). We do not retrieve vertical column density from
709 these fall slant column densities, because the resulting retrievals would be biased positive due to an
710 algorithm requirement that only positive BrO column densities are allowed in the optimal estimation
711 inversion. These differential slant column densities (dSCDs) can be used qualitatively to determine the
712 presence or absence of BrO above the detection limit. If the dSCDs display noise around zero at all
713 viewing angles, the BrO in the troposphere is below the detection limit of the spectrometer. A pattern of
714 larger BrO dSCDs at near-horizon viewing elevation angles indicating the presence of tropospheric BrO
715 above the detection limit is only observed at Utqiagvik during Arctic Spring (see Supplemental Figure
716 S12) . Any BrO present in the Arctic troposphere in September and October falls below detection limits at
717 Utqiagvik (see Supplemental Figure S12) and on each O-Buoy (see Supplemental Figure S13). The
718 average Arctic Spring 2015 MAX-DOAS BrO_{LTcol} detection limits are 5×10^{12} molecules/cm² (Peterson
719 et al., 2015; Simpson et al., 2017; Swanson et al., 2020). Both BLOW and PACK mechanisms lead to
720 prediction of increased fall BrO because the weather and sea ice conditions specified in the emission
721 algorithms occur in fall as well as spring.

722 Figure 9 shows fall predictions of BrO_{LTcol} filtered for times when solar elevation angle was
723 greater than 5°. BASE and PACK BrO_{LTcol} remain near zero in September but rise above the MAX-DOAS
724 detection limit of 5×10^{12} molecules/cm² BrO_{LTcol} in October. The addition of the blowing snow SSA
725 mechanism propels BLOW BrO_{LTcol} up to 6×10^{13} molecules/cm² in October. O-Buoys 13 and 14 have
726 the highest modeled fall BrO_{LTcol} but even Utqiagvik has several days of BrO_{LTcol} above 5×10^{12}
727 molecules/cm² in late October. There is no clear evidence of any BrO above MAX-DOAS detection limits
728 at Utqiagvik or on any O-Buoy in October, as seen by the dSCDs scattered around zero in Supplemental
729 Figures S12 and S13.

730



731

732 **Figure 9: Fall GEOS-Chem Predicted $\text{BrO}_{\text{LTcol}}$**

733 Hourly timeseries of BLOW+PACK, PACK, and BASE $\text{BrO}_{\text{LTcol}}$ on a) O-Buoy 10, b) O-Buoy 11, c) O-
 734 Buoy 12 and d) BARC at Utqiagvik during September and October 2015 BASE $\text{BrO}_{\text{LTcol}}$ in brown,
 735 BLOW $\text{BrO}_{\text{LTcol}}$ in yellow, PACK $\text{BrO}_{\text{LTcol}}$ in purple, and BLOW+PACK $\text{BrO}_{\text{LTcol}}$ in orange. All $\text{BrO}_{\text{LTcol}}$
 736 plotted continuously except for gaps where solar elevation angle was less than 5° .

737

738 Both mechanisms assume that snowpack and SSA are just as capable of recycling reactive
 739 bromine as in the springtime. High fall and winter SSA agrees with observations of peak SSA during
 740 polar winter in both Antarctica (Wagenbach et al., 1998) and in the Arctic (Jacobi et al., 2012). The
 741 deposition of Arctic haze (Douglas and Sturm, 2004) and SSA (Jacobi et al., 2019) increases snowpack
 742 salinity and sulfate content over the course of winter and spring. This seasonal change in snowpack
 743 salinity and acidity may enable reactive bromine recycling in the Arctic Spring, but there may not
 744 sufficient haze and SSA deposition in fall to decrease snowpack pH and increase snowpack bromide
 745 content. Additional observations of fall snowpack over sea ice including ion content could show different
 746 snowpack composition in spring and fall. Thus the GEOS-Chem model overestimates fall BrO by
 747 assuming the fall snowpack is equally capable of reactive bromine recycling as spring snowpack, possibly
 748 due to the assumption of an infinite reservoir of snowpack bromide in all seasons. Most other modeling

749 exercises have focused on spring with unknown predictions in fall, possibly indicating problems in
750 mechanisms or parameterizations being employed, so we suggest that modeling should be done for a full
751 year to improve underlying chemistry and physics. We also suggest a fall snow sampling campaign to
752 validate modeled fall BrO.

753 **6. Conclusions**

754 We add snowpack Br₂ production to GEOS-Chem based on multiple field observations
755 demonstrating molecular bromine production in snowpack interstitial air. We use a mechanistic
756 parameterization of snowpack Br₂ production based on Toyota et al. (2011) in which Br₂ is emitted from
757 all snowpack of sufficient salinity and depth over land and sea ice upon deposition of the precursor
758 species HOBr, BrNO₃, and ozone. Prior work has also added a blowing snow SSA production mechanism
759 that increases aerosol particulate bromide and thus facilitates heterogeneous recycling of reactive bromine
760 on these aerosol particle surfaces. We update the halogen scheme to GEOS-Chem 12.9.3 and performed
761 six model simulations including a BASE run with neither blowing snow SSA nor snowpack emissions, a
762 PACK run assuming constant yield of Br₂ on ozone deposition over all snow surfaces, a PHOTOPACK
763 run assuming increased daytime yield of Br₂ on ozone deposition (similar in Toyota et al., 2011), a
764 BLOW run using only blowing snow SSA formation and two additional runs combining BLOW and each
765 respective PACK mechanism. The increased daytime yield of Br₂ in PHOTOPACK leads to
766 overprediction of BrO in these simulations, but the PACK run (with constant Br₂ yield day and night)
767 matches monthly averaged BrO vertical column densities within measurement error for 9 of 13 cases at
768 O-Buoy and Utqiagvik in springtime months. The PACK and BLOW+PACK runs were successful in
769 replicating observed BrO events on O-Buoys in May. The BLOW mechanism effectively increases
770 aerosol surface available for turnover of reactive bromine. The snowpack mechanism has more impact on
771 modeled BrO mixing ratios than the blowing snow SSA mechanism, but both contribute to tropospheric
772 reactive bromine. We extend our model run to the full year and find that enhanced daytime Br₂ yield can
773 lead to increased Arctic Ocean Br₂ production in the summer. Examining modeled BrO in fall 2015
774 reveals prediction of BrO when using these mechanisms that are at odds with observations.

775 The inclusion of two Arctic reactive bromine production mechanisms based on literature
776 observations of snowpack Br₂ emission and blowing snow SSA formation improves model skill in
777 replicating Arctic tropospheric BrO in spring 2015. The snowpack is an important source of reactive
778 bromine, and SSA particles provide an abundant surface for sustained reactive bromine recycling in the
779 troposphere. We find that using both snowpack and blowing snow SSA bromine production mechanisms
780 is necessary for modeling BrO in the Arctic.

781

782 *Competing interests:* The authors declare that they have no conflict of interest.

783 Author contributions. WFS, WRS and CH designed the study. WRS collected and curated MAX-DOAS
784 data. KC, LM, JT, LJ, JH and contributed code for reactive bromine mechanisms. CH, KC, LJ, JH, BA,
785 SZ, QC, XW, and TS contributed model updates. WFS carried out modeling and analysis. WFS wrote the
786 paper with input from all authors.

787 **7. Acknowledgements**

788 We acknowledge support from the National Science Foundation for providing funding under grants ARC-
789 1602716, AGS-1702266, AGS-2109323, and ARC-1602883. This work also supported by the CNRS
790 INSU LEFE-CHAT program under the grant Brom-Arc, and NASA grant 80NSSC19K1273. This
791 research has received funding from the European Union's Horizon 2020 research and innovation program
792 under grant agreement no. 689443 via project iCUPE (Integrative and Comprehensive Understanding on
793 Polar Environments). The O-Buoy and Utqiagvik ground-based BrO datasets are available in the
794 arcticdata.io repository (doi:10.18739/A2WD4W). We recognize the work of Jiayue Huang in adding the
795 blowing snow SSA mechanism to GEOS-Chem. We would like to thank the National Oceanic and
796 Atmospheric Administration (NOAA) Global Monitoring Division for the provision of ozone and
797 temperature data near Utqiagvik available online at doi:10.7289/V57P8WBF. We acknowledge use of the
798 coastline distance dataset from the Pacific Islands Ocean Observing System. We acknowledge the use of
799 imagery from the Land Atmosphere Near Real-Time Capability for EOS (LANCE) system and services
800 from the Global Imagery Browse Services (GIBS), both operated by the NASA/GSFC/Earth Science Data
801 and Information System (ESDIS, <https://earthdata.nasa.gov>) with funding provided by NASA/HQ. We
802 owe a debt of gratitude to all members of the Atmospheric Chemistry and Global Change group at Florida
803 State University for their support for working with GEOS-Chem and Python. We thank the global GEOS-
804 Chem community for their tireless work to improve the model. We also thank all involved in the O-Buoy
805 project for data collection and analysis.

806 **8. References**

- 807 Alexander, B., Park, R. J., Jacob, D. J., Li, Q. B., Yantosca, R. M., Savarino, J., Lee, C. C. W. and
808 Thiemens, M. H.: Sulfate formation in sea-salt aerosols: Constraints from oxygen isotopes, *J. Geophys.*
809 *Res. D Atmos.*, 110(10), 1–12, doi:10.1029/2004JD005659, 2005.
- 810 AMAP: Arctic Monitoring and Assessment Program 2011: Mercury in the Arctic., 2011.
- 811 Artiglia, L., Edebeli, J., Orlando, F., Chen, S., Lee, M. T., Corral Arroyo, P., Gilgen, A., Bartels-Rausch,
812 T., Kleibert, A., Vazdar, M., Andres Carignano, M., Francisco, J. S., Shepson, P. B., Gladich, I. and
813 Ammann, M.: A surface-stabilized ozonide triggers bromide oxidation at the aqueous solution-vapour
814 interface, *Nat. Commun.*, 8(1), 1–7, doi:10.1038/s41467-017-00823-x, 2017.
- 815 Ayers, G. P., Gillett, R. W., Cainey, J. M. and Dick, A. L.: Chloride and bromide loss from sea-salt

816 particles in Southern Ocean air, *J. Atmos. Chem.*, 33(3), 299–319, doi:10.1023/A:1006120205159, 1999.

817 Bariteau, L., Helmig, D., Fairall, C. W., Hare, J. E., Hueber, J. and Lang, E. K.: Determination of oceanic
818 ozone deposition by ship-borne eddy covariance flux measurements, *Atmos. Meas. Tech.*, 3(2), 441–455,
819 doi:10.5194/amt-3-441-2010, 2010.

820 Barrie, L. A., Bottenheim, J. W., Schnell, R. C., Crutzen, P. J. and Rasmussen, R. A.: Ozone destruction
821 and photochemical reactions at polar sunrise in the lower Arctic atmosphere, *Nature*, 334(6178), 138–
822 141, doi:10.1038/334138a0, 1988.

823 Berg, W. W., Sperry, P. D., Rahn, K. A. and Gladney, E. S.: Atmospheric Bromine in the Arctic, *J.*
824 *Geophys. Res.*, 88(3), 6719–6736, doi:10.1029/JC088iC11p06719, 1983.

825 Bey, I., Jacob, D. J., Yantosca, R. M., Logan, J. A., Field, B. D., Fiore, A. M., Li, Q., Liu, H. Y., Mickley,
826 L. J. and Schultz, M. G.: Global modeling of tropospheric chemistry with assimilated meteorology:
827 Model description and evaluation, *J. Geophys. Res. Atmos.*, 106(D19), 23073–23095,
828 doi:10.1029/2001JD000807, 2001.

829 Bottenheim, J. W., Fuentes, J. D., Tarasick, D. W. and Anlauf, K. G.: Ozone in the Arctic lower
830 troposphere during winter and spring 2000 (ALERT2000), *Atmos. Environ.*, 36, 2535–2544, 2002.

831 Burd, J. A., Peterson, P. K., Nghiem, S. V., Perovich, D. K. and Simpson, W. R.: Snow Melt Onset
832 Hinders Bromine Monoxide Heterogeneous Recycling in the Arctic, *J. Geophys. Res. Atmos.*, 1–13,
833 doi:10.1002/2017JD026906, 2017.

834 Cao, L., Platt, U. and Gutheil, E.: Role of the boundary layer in the occurrence and termination of the
835 tropospheric ozone depletion events in polar spring, *Atmos. Environ.*, 132, 98–110,
836 doi:10.1016/j.atmosenv.2016.02.034, 2016.

837 Carlson, D., Donohoue, D., Platt, U. and Simpson, W. R.: A low power automated MAX-DOAS
838 instrument for the Arctic and other remote unmanned locations, *Atmos. Meas. Tech.*, 429–439, 2010.

839 Chance, K.: Analysis of BrO Measurements from the Global Ozone Monitoring Experiment, *Geophys.*
840 *Res. Lett.*, 25(17), 3335–3338, 1998.

841 Chen, Q., Schmidt, J. A., Shah, V., Jaeglé, L., Sherwen, T. and Alexander, B.: Sulfate production by
842 reactive bromine: Implications for the global sulfur and reactive bromine budgets, *Geophys. Res. Lett.*,
843 44(13), 7069–7078, doi:10.1002/2017GL073812, 2017.

844 Choi, S., Wang, Y., Salawitch, R. J., Canty, T., Joiner, J., Zeng, T., Kurosu, T. P., Chance, K., Richter,
845 A., Huey, L. G., Liao, J., Neuman, J. A., Nowak, J. B., Dibb, J. E., Weinheimer, A. J., Diskin, G.,
846 Ryerson, T. B., Da Silva, A., Curry, J., Kinnison, D., Tilmes, S. and Levelt, P. F.: Analysis of satellite-
847 derived Arctic tropospheric BrO columns in conjunction with aircraft measurements during ARCTAS and
848 ARCPAC, *Atmos. Chem. Phys.*, 12(3), 1255–1285, doi:10.5194/acp-12-1255-2012, 2012.

849 von Clarmann, T. and Glatthor, N.: The application of mean averaging kernels to mean trace gas
850 distributions, *Atmos. Meas. Tech. Discuss.*, 1–11, doi:10.5194/amt-2019-61, 2019.

851 Clemer, K., Van Roozendaal, M., Fayt, C., Hendrick, F., Hermans, C., Pinardi, G., Spurr, R., Wang, P.
852 and Maziere, M. De: Multiple wavelength retrieval of tropospheric aerosol optical properties from
853 MAXDOAS measurements in Beijing, *Atmos. Meas. Tech.*, 3, 863–878, doi:10.5194/amt-3-863-2010,
854 2010.

855 Custard, K. D., Raso, A. R. W., Shepson, P. B., Staebler, R. M. and Pratt, K. A.: Production and Release
856 of Molecular Bromine and Chlorine from the Arctic Coastal Snowpack, *ACS Earth Sp. Chem.*, 1, 142–
857 151, doi:10.1021/acsearthspacechem.7b00014, 2017.

- 858 Dery, S. J. and Yau, M. K.: A Bulk Blowing Snow Model, *Bound. Layer Meteorol.*, 93, 237–251, 1999.
- 859 Déry, S. J. and Yau, M. K.: Simulation of blowing snow in the Canadian Arctic using a double-moment
860 model, *Boundary-Layer Meteorol.*, 99(2), 297–316, doi:10.1023/A:1018965008049, 2001.
- 861 Domine, F., Sparapani, R., Ianniello, A. and Beine, H. J.: The origin of sea salt in snow on Arctic sea ice
862 and in coastal regions, *Atmos. Chem. Phys. Discuss.*, 4(4), 4737–4776, doi:10.5194/acpd-4-4737-2004,
863 2004.
- 864 Douglas, T. A. and Sturm, M.: Arctic haze, mercury and the chemical composition of snow across
865 northwestern Alaska, *Atmos. Environ.*, doi:10.1016/j.atmosenv.2003.10.042, 2004.
- 866 Eastham, S. D., Weisenstein, D. K. and Barrett, S. R. H.: Development and evaluation of the unified
867 tropospheric-stratospheric chemistry extension (UCX) for the global chemistry-transport model GEOS-
868 Chem, *Atmos. Environ.*, 89, 52–63, doi:10.1016/j.atmosenv.2014.02.001, 2014.
- 869 Falk, S. and Sinnhuber, B. M.: Polar boundary layer bromine explosion and ozone depletion events in the
870 chemistry-climate model EMAC v2.52: Implementation and evaluation of AirSnow algorithm, *Geosci.*
871 *Model Dev.*, 11(3), 1115–1131, doi:10.5194/gmd-11-1115-2018, 2018.
- 872 Fan, S. M. and Jacob, D. J.: Surface ozone depletion in Arctic spring sustained by bromine reactions on
873 aerosols, *Nature*, 359(6395), 522–524, doi:10.1038/359522a0, 1992.
- 874 Fischer, E. V., Jacob, D. J., Yantosca, R. M., Sulprizio, M. P., Millet, D. B., Mao, J., Paulot, F., Singh, H.
875 B., Roiger, A., Ries, L., Talbot, R. W., Dzepina, K. and Pandey Deolal, S.: Atmospheric peroxyacetyl
876 nitrate (PAN): A global budget and source attribution, *Atmos. Chem. Phys.*, 14(5), 2679–2698,
877 doi:10.5194/acp-14-2679-2014, 2014.
- 878 Fisher, J. A., Jacob, D. J., Travis, K. R., Kim, P. S., Marais, E. A., Miller, C. C., Yu, K., Zhu, L.,
879 Yantosca, R. M., Sulprizio, M. P., Mao, J., Wennberg, P. O., Crounse, J. D., Teng, A. P., Nguyen, T. B.,
880 Clair, J. M. S., Cohen, R. C., Romer, P., Nault, B. A., Wooldridge, P. J., Jimenez, J. L., Campuzano-Jost,
881 P., Day, D. A., Hu, W., Shepson, P. B., Xiong, F., Blake, D. R., Goldstein, A. H., Misztal, P. K., Hanisco,
882 T. F., Wolfe, G. M., Ryerson, T. B., Wisthaler, A. and Mikoviny, T.: Organic nitrate chemistry and its
883 implications for nitrogen budgets in an isoprene- and monoterpene-rich atmosphere: Constraints from
884 aircraft (SEAC4RS) and ground-based (SOAS) observations in the Southeast US, *Atmos. Chem. Phys.*,
885 16(9), 5969–5991, doi:10.5194/acp-16-5969-2016, 2016.
- 886 Foster, K. L., Plastridge, R. A., Bottenheim, J. W., Shepson, P. B., Finlayson-pitts, B. J. and Spicer, C.
887 W.: The Role of Br₂ and BrCl in Surface Ozone Destruction at Polar Sunrise, *Science* (80-.),
888 291(JANUARY), 471–475, 2001.
- 889 Frey, M. M., Norris, S. J., Brooks, I. M., Anderson, P. S., Nishimura, K., Yang, X., Jones, A. E.,
890 Nerentorp Mastromonaco, M. G., Jones, D. H. and Wolff, E. W.: First direct observation of sea salt
891 aerosol production from blowing snow above sea ice, *Atmos. Chem. Phys.*, (April), 1–53,
892 doi:10.5194/acp-2019-259, 2020.
- 893 Frieß, U., Monks, P. S., Remedios, J. J., Rozanov, A., Sinreich, R., Wagner, T. and Platt, U.: MAX-
894 DOAS O₄ measurements: A new technique to derive information on atmospheric aerosols: 2. Modeling
895 studies, *J. Geophys. Res.*, 111, 20, doi:10.1029/2005JD006618, 2006.
- 896 Frieß, U., Beirle, S., Bonilla, L. A., Bösch, T., Friedrich, M. M., Hendrick, F., Piders, A., Richter, A.,
897 Roozendael, M. Van, Rozanov, V. V., Spinei, E. and Tirpitz, J.: Intercomparison of MAX-DOAS vertical
898 profile retrieval algorithms : studies using synthetic data, *Atmos. Meas. Tech.*, (2), 2155–2181, 2019.
- 899 Gelaro, R., McCarty, W., Suarez, M. J., Todling, R., Molod, A., Takacs, L., Randles, C., Darmenov, A.,
900 Bosilovich, M., Reichle, R., Wargan, K., Coy, L., Cullather, R., Draper, C., Akella, S., Buchard, V.,

901 Conaty, A., Da Silva, A., Gu, W., Kim, G., Koster, R., Lucchesi, R., Merkova, D., Nielsen, J. E., Partyka,
902 G., Pawson, S., Putman, W., Rienecker, M., Schubert, S., Sienkiewicz, M. and Zhao, B.: The Modern-Era
903 Retrospective Analysis for Research and Applications , *J. Clim.*, 30, 5419–5454, doi:10.1175/JCLI-D-16-
904 0758.1, 2017.

905 Group, N. O. B. P. and Stumpf, R.: Distance to Nearest Coastline: 0.01 Degree Grid, [online] Available
906 from: https://pae-paha.pacioos.hawaii.edu/thredds/ncss/dist2coast_1deg/dataset.html, 2021.

907 Halfacre, J. W., Knepp, T. N., Shepson, P. B., Thompson, C. R., Pratt, K. A., Li, B., Peterson, P. K.,
908 Walsh, S. J., Simpson, W. R., Matrai, P. A., Bottenheim, J. W., Netcheva, S., Perovich, D. K. and Richter,
909 A.: Temporal and spatial characteristics of ozone depletion events from measurements in the Arctic,
910 *Atmos. Chem. Phys.*, 14(10), 4875–4894, doi:10.5194/acp-14-4875-2014, 2014.

911 Halfacre, J. W., Shepson, P. B. and Pratt, K. A.: pH-dependent production of molecular chlorine,
912 bromine, and iodine from frozen saline surfaces, *Atmos. Chem. Phys.*, 19, 4917–4931, 2019.

913 Hara, K., Osada, K., Yabuki, M., Takashima, H., Theys, N. and Yamanouchi, T.: Important contributions
914 of sea-salt aerosols to atmospheric bromine cycle in the Antarctic coasts, *Sci. Rep.*, 8(1),
915 doi:10.1038/s41598-018-32287-4, 2018.

916 Herrmann, M., Sihler, H., Frieß, U., Wagner, T., Platt, U. and Gutheil, E.: Time-dependent 3D
917 simulations of tropospheric ozone depletion events in the Arctic spring using the Weather Research and
918 Forecasting model coupled with Chemistry (WRF-Chem), , 7611–7638, 2021.

919 Holmes, C. D., Jacob, D. J., Corbitt, E. S., Mao, J., Yang, X., Talbot, R. and Slemr, F.: Global
920 atmospheric model for mercury including oxidation by bromine atoms, *Atmos. Chem. Phys.*, 10(24),
921 12037–12057, doi:10.5194/acp-10-12037-2010, 2010.

922 Hönninger, G. and Platt, U.: Observations of BrO and its vertical distribution during surface ozone
923 depletion at Alert, *Atmos. Environ.*, 36(15–16), 2481–2489, doi:10.1016/S1352-2310(02)00104-8, 2002.

924 Hönninger, G., von Friedeburg, C. and Platt, U.: Multi Axis Differential Optical Absorption Spectroscopy
925 (MAX-DOAS), *Atmos. Chem. Phys.*, 4, 231–254, doi:10.5194/acpd-3-5595-2003, 2004.

926 Huang, J. and Jaeglé, L.: Wintertime enhancements of sea salt aerosol in polar regions consistent with a
927 sea-ice source from blowing snow, *Atmos. Chem. Phys.*, (November), 1–23, doi:10.5194/acp-2016-972,
928 2017.

929 Huang, J., Jaeglé, L. and Shah, V.: Using CALIOP to constrain blowing snow emissions of sea salt
930 aerosols over Arctic and Antarctic sea ice, *Atmos. Chem. Phys.*, 16253–16269, 2018.

931 Huang, J., Jaeglé, L., Chen, Q., Alexander, B., Sherwen, T., Evans, M., Theys, N. and Choi, S.:
932 Evaluating the impact of blowing snow sea salt aerosol on springtime BrO and O₃ in the Arctic, *Atmos.*
933 *Chem. Phys.*, 1–36, doi:10.5194/acp-2019-1094, 2020.

934 Jacobi, H. W., Voisin, D., Jaffrezo, J. L., Cozic, J. and Douglas, T. A.: Chemical composition of the
935 snowpack during the OASIS spring campaign 2009 at Barrow, Alaska, *J. Geophys. Res. Atmos.*,
936 doi:10.1029/2011JD016654, 2012.

937 Jacobi, H. W., Oblitner, F., Da Costa, S., Ginot, P., Eleftheriadis, K., Aas, W. and Zanatta, M.:
938 Deposition of ionic species and black carbon to the Arctic snowpack: Combining snow pit observations
939 with modeling, *Atmos. Chem. Phys.*, 19(15), 10361–10377, doi:10.5194/acp-19-10361-2019, 2019.

940 Jaeglé, L., Quinn, P. K., Bates, T. S., Alexander, B. and Lin, J. T.: Global distribution of sea salt aerosols:
941 New constraints from in situ and remote sensing observations, *Atmos. Chem. Phys.*, 11(7), 3137–3157,
942 doi:10.5194/acp-11-3137-2011, 2011.

943 Keller, C. A., Long, M. S., Yantosca, R. M., Da Silva, A. M., Pawson, S. and Jacob, D. J.: HEMCO v1.0:
944 A versatile, ESMF-compliant component for calculating emissions in atmospheric models, *Geosci. Model*
945 *Dev.*, 7(4), 1409–1417, doi:10.5194/gmd-7-1409-2014, 2014.

946 Knepp, T. N., Bottenheim, J., Carlsen, M., Carlson, D., Donohoue, D., Friederich, G., Matrai, P. A.,
947 Netcheva, S., Perovich, D. K., Santini, R., Shepson, P. B., Simpson, W., Valentig, T., Williams, C. and
948 Wyss, P. J.: Development of an autonomous sea ice tethered buoy for the study of ocean-atmosphere-sea
949 ice-snow pack interactions: The O-buoy, *Atmos. Meas. Tech.*, 3(1), 249–261, doi:10.5194/amt-3-249-
950 2010, 2010.

951 Koo, J. H., Wang, Y., Kurosu, T. P., Chance, K., Rozanov, A., Richter, A., Oltmans, S. J., Thompson, A.
952 M., Hair, J. W., Fenn, M. A., Weinheimer, A. J., Ryerson, T. B., Solberg, S., Huey, L. G., Liao, J., Dibb,
953 J. E., Neuman, J. A., Nowak, J. B., Pierce, R. B., Natarajan, M. and Al-Saadi, J.: Characteristics of
954 tropospheric ozone depletion events in the Arctic spring: Analysis of the ARCTAS, ARCPAC, and
955 ARCIONS measurements and satellite BrO observations, *Atmos. Chem. Phys.*, 12(20), 9909–9922,
956 doi:10.5194/acp-12-9909-2012, 2012.

957 Krnavek, L., Simpson, W. R., Carlson, D., Domine, F., Douglas, T. A. and Sturm, M.: The chemical
958 composition of surface snow in the Arctic: Examining marine, terrestrial, and atmospheric influences,
959 *Atmos. Environ.*, 50, 349–359, doi:10.1016/j.atmosenv.2011.11.033, 2012.

960 De Leeuw, G., Andreas, E. L., Anguelova, M. D., Fairall, C. W., Lewis, E. R., O’Dowd, C., Schulz, M.
961 and Schwartz, S. E.: Production flux of sea spray aerosol, *Rev. Geophys.*, 49(2), 1–39,
962 doi:10.1029/2010RG000349, 2011.

963 Lehrer, E., Hönninger, G. and Platt, U.: A one dimensional model study of the mechanism of halogen
964 liberation and vertical transport in the polar troposphere, *Atmos. Chem. Phys.*, 4(11/12), 2427–2440,
965 doi:10.5194/acp-4-2427-2004, 2004.

966 Lewis, E. R. and Schwartz, S. E.: *Salt Aerosol Production: Mechanisms, Methods, Measurements, and*
967 *Models: A Critical Review*, American Geophysical Union, Washington D.C., 2004.

968 Lin, H., Jacob, D. J., Lundgren, E. W., Sulprizio, M. P., Keller, C. A., Fritz, T. M., Eastham, S. D.,
969 Emmons, L. K., Campbell, P. C., Baker, B., Saylor, R. D. and Montuoro, R.: Harmonized Emissions
970 Component (HEMCO) 3.0 as a versatile emissions component for atmospheric models: Application in the
971 GEOS-Chem, NASA GEOS, WRF-GC, CESM2, NOAA GEFS-Aerosol, and NOAA UFS models,
972 *Geosci. Model Dev.*, 14(9), 5487–5506, doi:10.5194/gmd-14-5487-2021, 2021.

973 Liu, T., Chan, A. W. H. and Abbatt, J. P. D.: Multiphase Oxidation of Sulfur Dioxide in Aerosol
974 Particles: Implications for Sulfate Formation in Polluted Environments, *Environ. Sci. Technol.*,
975 *acs.est.0c06496*, doi:10.1021/acs.est.0c06496, 2021.

976 Mao, J., Paulot, F., Jacob, D. J., Cohen, R. C., Crouse, J. D., Wennberg, P. O., Keller, C. A., Hudman,
977 R. C., Barkley, M. P. and Horowitz, L. W.: Ozone and organic nitrates over the eastern United States:
978 Sensitivity to isoprene chemistry, *J. Geophys. Res. Atmos.*, 118(19), 11256–11268,
979 doi:10.1002/jgrd.50817, 2013.

980 Marelle, L., Thomas, J. L., Ahmed, S., Tuite, K., Stutz, J., Dommergue, A., Simpson, W. R., Frey, M. M.
981 and Baladima, F.: Implementation and Impacts of Surface and Blowing Snow Sources of Arctic Bromine
982 Activation Within WRF-Chem 4.1.1, *J. Adv. Model. Earth Syst.*, 13(8), doi:10.1029/2020ms002391,
983 2021.

984 McClure-Begley, A., Petropavlovskikh, I. and Oltmans, S.: NOAA Global Monitoring Surface Ozone
985 Network. 1973-2014. National Oceanic and Atmospheric Administration, Earth Systems Research
986 Laboratory Global Monitoring Division. Boulder, CO, , doi:10.7289/V57P8WBF, 2014.

987 Mcnamara, S. M., Kolesar, K. R., Wang, S., Kirpes, R. M., May, N. W., Gunsch, M. J., Cook, R. D.,
988 Fuentes, J. D., Hornbrook, R. S., Apel, E. C., Laskin, A. and Pratt, K. A.: Observation of Road Salt
989 Aerosol Driving Inland Wintertime Atmospheric Chlorine Chemistry, *ACS Cent. Sci.*, 6(684–694),
990 doi:10.1021/acscentsci.9b00994, 2020.

991 Moore, C. W., Obrist, D., Steffen, A., Staebler, R. M., Douglas, T. A., Richter, A. and Nghiem, S. V:
992 Convective forcing of mercury and ozone in the Arctic boundary layer induced by leads in sea ice.,
993 *Nature*, 506(7486), 81–4, doi:10.1038/nature12924, 2014.

994 Nghiem, S.: Studying bromine, ozone, and mercury chemistry in the Arctic, *Eos, Trans. Am. Geophys.*
995 *Union*, 94(33), 289–291, doi:10.1038/NGEO1779., 2013.

996 Oltmans, S. J., Johnson, B. J. and Harris, J. M.: Springtime boundary layer ozone depletion at Barrow,
997 Alaska: Meteorological influence, year-to-year variation, and long-term change, *J. Geophys. Res. Atmos.*,
998 117(8), 1–18, doi:10.1029/2011JD016889, 2012.

999 Oum, K. W., Lakin, M. J. and Finlayson-Pitts, B. J.: Bromine activation in the troposphere by the dark
1000 reaction of O₃ with seawater ice, *Geophys. Res. Lett.*, 25(21), 3923–3926, doi:10.1029/1998GL900078,
1001 1998.

1002 Parrella, J. P., Jacob, D. J., Liang, Q., Zhang, Y., Mickley, L. J., Miller, B., Evans, M. J., Yang, X., Pyle,
1003 J. A., Theys, N. and Van Roozendaal, M.: Tropospheric bromine chemistry: Implications for present and
1004 pre-industrial ozone and mercury, *Atmos. Chem. Phys.*, 12(15), 6723–6740, doi:10.5194/acp-12-6723-
1005 2012, 2012.

1006 Peterson, P. K., Simpson, W. R., Pratt, K. A., Shepson, P. B., Frieß, U., Zielcke, J., Platt, U., Walsh, S. J.
1007 and Nghiem, S. V.: Dependence of the vertical distribution of bromine monoxide in the lower troposphere
1008 on meteorological factors such as wind speed and stability, *Atmos. Chem. Phys.*, 15, 2119–2137,
1009 doi:10.5194/acp-15-2119-2015, 2015.

1010 Peterson, P. K., Pöhler, D., Sihler, H., Zielcke, J., General, S., Frieß, U., Platt, U., Simpson, W. R.,
1011 Nghiem, S. V., Shepson, P. B., Stirm, B. H., Dhaniyala, S., Wagner, T., Caulton, D. R., Fuentes, J. D. and
1012 Pratt, K. A.: Observations of bromine monoxide transport in the Arctic sustained on aerosol particles,
1013 *Atmos. Chem. Phys.*, 17(12), 7567–7579, doi:10.5194/acp-17-7567-2017, 2017.

1014 Peterson, P. K., Pöhler, D., Zielcke, J., General, S., Friess, U., Platt, U., Simpson, W. R., Nghiem, S.,
1015 Shepson, P. B., Stirm, B. H. and Pratt, K. A.: Springtime Bromine Activation Over Coastal and Inland
1016 Arctic Snowpacks, *ACS Earth Sp. Chem.*, acsearthspacechem.8b00083,
1017 doi:10.1021/acsearthspacechem.8b00083, 2018.

1018 Peterson, P. K., Hartwig, M., May, N. W., Schwartz, E., Rigor, I., Ermold, W., Steele, M., Morison, J. H.,
1019 Nghiem, S. V and Pratt, K. A.: Snowpack measurements suggest role for multi-year sea ice regions in
1020 Arctic atmospheric bromine and chlorine chemistry, *Elementa*, 2019.

1021 Pöhler, D., Vogel, L., Friess, U. and Platt, U.: Observation of halogen species in the Amundsen Gulf,
1022 Arctic, by active long-path differential optical absorption spectroscopy., *Proc. Natl. Acad. Sci. U. S. A.*,
1023 107(15), 6582–7, doi:10.1073/pnas.0912231107, 2010.

1024 Pound, R. J., Sherwen, T., Helmig, D., Carpenter, L. J. and Evans, M. J.: Influences of oceanic ozone
1025 deposition on tropospheric photochemistry, *Atmos. Chem. Phys.*, 20(7), 4227–4239, doi:10.5194/acp-20-
1026 4227-2020, 2020.

1027 Pratt, K. A., Custard, K. D., Shepson, P. B., Douglas, T. A., Pöhler, D., General, S., Zielcke, J., Simpson,
1028 W. R., Platt, U., Tanner, D. J., Gregory Huey, L., Carlsen, M. and Stirm, B. H.: Photochemical production
1029 of molecular bromine in Arctic surface snowpacks, *Nat. Geosci.*, 6(5), 351–356, doi:10.1038/ngeo1779,

- 1030 2013.
- 1031 Richter, A., Wittrock, F., Eisinger, M. and Burrows, J. P.: GOME observations of tropospheric BrO in
1032 Northern Hemispheric spring and summer 1997, *Geophys. Res. Lett.*, 25(14), 2683–2686,
1033 doi:10.1029/98GL52016, 1998.
- 1034 Rodgers, C. D. and Connor, B. J.: Intercomparison of remote sounding instruments, *J. Geophys. Res.*,
1035 108(March 2002), doi:10.1029/2002JD002299, 2003.
- 1036 Saiz-Lopez, A. and von Glasow, R.: Reactive halogen chemistry in the troposphere, *Chem. Soc. Rev.*,
1037 41(19), 6448, doi:10.1039/c2cs35208g, 2012.
- 1038 Salawitch, R. J., Canty, T., Kurosu, T., Chance, K., Liang, Q., Silva, A., Pawson, S., Nielsen, J. E.,
1039 Rodriguez, J. M., Bhartia, P. K., Liu, X., Huey, L. G., Liao, J., Stickel, R. E., Tanner, D. J., Dibb, J. E.,
1040 Simpson, W. R., Donohoue, D., Kreher, K., Johnston, P. V., Gao, R. S., Johnson, B., Bui, T. P. and Chen,
1041 G.: A new interpretation of total column BrO during Arctic spring, *Geophys. Res. Lett.*, 37(21), 1–9,
1042 doi:10.1029/2010GL043798, 2010.
- 1043 Sander, R., Keene, W. C., Pszenny, A. A. P., Arimoto, R., Ayers, G. P., Baboukas, E., Caaney, J. M.,
1044 Crutzen, P. J., Duce, R. A., Hönninger, G., Huebert, B. J., Maenhaut, W., Mihalopoulos, N., Turekian, V.
1045 C. and Van Dingenen, R.: Inorganic bromine in the marine boundary layer: A critical review, *Atmos.*
1046 *Chem. Phys.*, 3(5), 1301–1336, doi:10.5194/acp-3-1301-2003, 2003.
- 1047 Schmidt, J. A., Jacob, D. J., Horowitz, H. M., Hu, L., Sherwen, T., Evans, M. J., Liang, Q., Suleiman, R.
1048 M., Oram, D. E., Le Breton, M., Percival, C. J., Wang, S., Dix, B. and Volkamer, R.: Modeling the
1049 observed tropospheric BrO background: Importance of multiphase chemistry and implications for ozone,
1050 OH, and mercury, *J. Geophys. Res.*, 121(19), 11819–11835, doi:10.1002/2015JD024229, 2016.
- 1051 Schroeder, W. H., Anlauf, K. G., Barrie, L. A., Lu, J. Y. and Steffen, A.: Arctic Springtime Depletion of
1052 Mercury, *Nature*, 394, 331–332, doi:10.1038/379126b0, 1998.
- 1053 Shah, V., Jacob, D. J., Moch, J. M., Wang, X. and Zhai, S.: Global modeling of cloud water acidity ,
1054 precipitation acidity , and acid inputs to ecosystems, *Atmos. Chem. Phys.*, 12223–12245, 2020.
- 1055 Sherwen, T., Schmidt, J. A., Evans, M. J., Carpenter, L. J., Großmann⁴, K., Eastham, S. D., J., D. J., Dix,
1056 B., Koenig, T. K., Sinreich, R., Ortega, I., Volkamer, R., Saiz-Lopez, A., Prados-Roman, C., Mahajan, A.
1057 S. and C. Ordóñez: DISCUSS Global impacts of tropospheric halogens (Cl, Br, I) on oxidants and
1058 composition in GEOS-Chem, *Atmos. Chem. Phys. Discuss.*, (May), doi:10.5194/acp-2016-424, 2016a.
- 1059 Sherwen, T., Schmidt, J. A., Evans, M. J., Carpenter, L. J., Großmann, K., Eastham, S. D., Jacob, D. J.,
1060 Dix, B., Koenig, T. K., Sinreich, R., Ortega, I., Volkamer, R., Saiz-Lopez, A., Prados-Roman, C.,
1061 Mahajan, A. S. and Ordóñez, C.: Global impacts of tropospheric halogens (Cl, Br, I) on oxidants and
1062 composition in GEOS-Chem, *Atmos. Chem. Phys.*, 16(18), 12239–12271, doi:10.5194/acp-16-12239-
1063 2016, 2016b.
- 1064 Sherwen, T., Evans, M. J., Carpenter, L. J., Schmidt, J. A. and Mickely, L. J.: Halogen chemistry reduces
1065 tropospheric O₃ radiative forcing, *Atmos. Chem. Phys.*, (August), 1–18, doi:10.5194/acp-2016-688,
1066 2016c.
- 1067 Simpson, W. R.: Atmospheric measurements via Multiple Axis Differential Optical Absorption
1068 Spectroscopy (MAXDOAS), Utqiagvik (Barrow), Alaska 2012-2018. Arctic Data Center, Arcticdata.io,
1069 doi:10.18739/A2222R550, 2018.
- 1070 Simpson, W. R., Perovich, D. K., Matrai, P. A., Shepson, P. B. and Chavez, F.: The Collaborative O-
1071 Buoy Project: Deployment of a Network of Arctic Ocean Chemical Sensors for the IPY and beyond.
1072 Arctic Data Center, , doi:10.18739/A2WD4W, 2009.

- 1073 Simpson, W. R., Brown, S. S., Saiz-Lopez, A., Thornton, J. A. and Glasow, R. Von: Tropospheric
 1074 Halogen Chemistry: Sources, Cycling, and Impacts, *Chem. Rev.*, 150312153236002,
 1075 doi:10.1021/cr5006638, 2015.
- 1076 Simpson, W. R., Peterson, P. K., Frieß, U., Sihler, H., Lampel, J., Platt, U., Moore, C., Pratt, K., Shepson,
 1077 P., Halfacre, J. and Nghiem, S. V: Horizontal and vertical structure of reactive bromine events probed by
 1078 bromine monoxide MAX-DOAS, *Atmos. Chem. Phys.*, 17, 9291–9309, 2017.
- 1079 Stutz, J., Thomas, J. L., Hurlock, S. C., Schneider, M., Von Glasow, R., Piot, M., Gorham, K., Burkhart,
 1080 J. F., Ziemba, L., Dibb, J. E. and Lefer, B. L.: Longpath DOAS observations of surface BrO at Summit,
 1081 Greenland, *Atmos. Chem. Phys.*, 11(18), 9899–9910, doi:10.5194/acp-11-9899-2011, 2011.
- 1082 Swanson, W. F., Graham, K. A., Halfacre, J. W., Holmes, C. D., Shepson, P. B. and Simpson, W. R.:
 1083 Arctic Reactive Bromine Events Occur in Two Distinct Sets of Environmental Conditions : A Statistical
 1084 Analysis of 6 Years of Observations *Journal of Geophysical Research : Atmospheres*, , 1–19,
 1085 doi:10.1029/2019JD032139, 2020.
- 1086 Tang, T. and McConnell, J. C.: Autocatalytic release of bromine from Arctic snow pack during polar
 1087 sunrise, *Geophys. Res. Lett.*, 23(19), 2633–2636, doi:10.1029/96GL02572, 1996.
- 1088 Theys, N., Van Roozendaal, M., Hendrick, F., Yang, X., De Smedt, I., Richter, A., Begoin, M., Errera,
 1089 Q., Johnston, P. V., Kreher, K. and De Maziere, M.: Global observations of tropospheric BrO columns
 1090 using GOME-2 satellite data, *Atmos. Chem. Phys.*, 11(4), 1791–1811, doi:10.5194/acp-11-1791-2011,
 1091 2011.
- 1092 Thomas, J. L., Stutz, J., Lefer, B., Huey, L. G., Toyota, K., Dibb, J. E. and Von Glasow, R.: Modeling
 1093 chemistry in and above snow at Summit, Greenland - Part 1: Model description and results, *Atmos.*
 1094 *Chem. Phys.*, 11(10), 4899–4914, doi:10.5194/acp-11-4899-2011, 2011.
- 1095 Toom-Sauntry, D. and Barrie, L. A.: Chemical composition of snowfall in the high Arctic: 1990-1994,
 1096 *Atmos. Environ.*, 36(15–16), 2683–2693, doi:10.1016/S1352-2310(02)00115-2, 2002.
- 1097 Toyota, K., McConnell, J. C., Lupu, A., Neary, L., McLinden, C. A., Richter, A., Kwok, R., Semeniuk,
 1098 K., Kaminski, J. W., Gong, S.-L., Jarosz, J., Chipperfield, M. P. and Sioris, C. E.: Analysis of reactive
 1099 bromine production and ozone depletion in the Arctic boundary layer using 3-D simulations with GEM-
 1100 AQ: inference from synoptic-scale patterns, *Atmos. Chem. Phys.*, 11(8), 3949–3979, doi:10.5194/acp-11-
 1101 3949-2011, 2011.
- 1102 Toyota, K., McConnell, J. C., Staebler, R. M. and Dastoor, A. P.: Air – snowpack exchange of bromine ,
 1103 ozone and mercury in the springtime Arctic simulated by the 1-D model PHANTAS – Part 1 : In-snow
 1104 bromine activation and its impact on ozone, *Atmos. Chem. Phys.*, 4101–4133, doi:10.5194/acp-14-4101-
 1105 2014, 2014.
- 1106 Travis, K. R., Jacob, D. J., Fisher, J. A., Kim, P. S., Marais, E. A., Zhu, L., Yu, K., Miller, C. C.,
 1107 Yantosca, R. M., Sulprizio, M. P., Thompson, A. M., Wennberg, P. O., Crounse, J. D., St Clair, J. M.,
 1108 Cohen, R. C., Laughner, J. L., Dibb, J. E., Hall, S. R., Ullmann, K., Wolfe, G. M., Pollack, I. B., Peischl,
 1109 J., Neuman, J. A. and Zhou, X.: Why do models overestimate surface ozone in the Southeast United
 1110 States?, *Atmos. Chem. Phys.*, 16(21), 13561–13577, doi:10.5194/acp-16-13561-2016, 2016.
- 1111 Vogt, R., Crutzen, P. and Sander, R.: A mechanism for halogen release from sea-salt, *Nature*,
 1112 383(September), 327–331, 1996.
- 1113 Wagenbach, D., Minikin, A., Ducroz, F., Mulvaney, R., Keck, L., Legrand, M., Hall, J. S. and Wolff, E.
 1114 W.: Sea-salt aerosol in coastal Antarctic regions at three coastal, *J. Geophys. Res. Atmos.*, 103, 961–974,
 1115 1998.

- 1116 Wagner, T. and Platt, U.: Satellite mapping of enhanced BrO concentrations in the troposphere, *Nature*,
1117 395(October), 486–490, doi:10.1038/26723, 1998.
- 1118 Wang, S. and Pratt, K. A.: Molecular Halogens Above the Arctic Snowpack: Emissions, Diurnal
1119 Variations, and Recycling Mechanisms, *J. Geophys. Res. Atmos.*, 122(21), 11,991–12,007,
1120 doi:10.1002/2017JD027175, 2017.
- 1121 Wang, S., Mcnamara, S. M., Moore, C. W., Obrist, D., Steffen, A., Shepson, P. B., Staebler, R. M., Raso,
1122 A. R. W. and Pratt, K. A.: Direct detection of atmospheric atomic bromine leading to mercury and ozone
1123 depletion, *Proc. Natl. Acad. Sci.*, 116(29), doi:10.18739/A2D79598P.1, 2019a.
- 1124 Wang, X., Jacob, D. J., Eastham, S. D., Sulprizio, M. P., Zhu, L., Chen, Q., Alexander, B., Sherwen, T.,
1125 Evans, M. J., Lee, B. H., Haskins, J. D., Lopez-hilfiker, F. D., Thornton, J. A., Huey, G. L. and Liao, H.:
1126 The role of chlorine in global tropospheric chemistry, *Atmos. Chem. Phys.*, 3981–4003, 2019b.
- 1127 Wang, X., Jacob, D. J., Downs, W., Zhai, S., Zhu, L., Shah, V., Holmes, C. D., Sherwen, T., Alexander,
1128 B., Evans, M. J., Eastham, S. D., Neuman, J. A., Veres, P. R., Koenig, T. K., Volkamer, R., Huey, L. G.,
1129 Bannan, T. J., Percival, C. J., Lee, B. H. and Thornton, J. A.: Global tropospheric halogen (Cl, Br, I)
1130 chemistry and its impact on oxidants, *Atmos. Chem. Phys.*, 21(18), 13973–13996, doi:10.5194/acp-21-
1131 13973-2021, 2021.
- 1132 Wennberg, P. O.: Bromine explosion, *Nature*, 397(6717), 299–301, doi:10.1038/16805, 1999.
- 1133 Wren, S. N., Kahan, T. F., Jumaa, K. B. and Donaldson, D. J.: Spectroscopic studies of the heterogeneous
1134 reaction between O₃(g) and halides at the surface of frozen salt solutions, *J. Geophys. Res. Atmos.*,
1135 115(16), 1–8, doi:10.1029/2010JD013929, 2010.
- 1136 Wren, S. N., Donaldson, D. J. and Abbatt, J. P. D.: Photochemical chlorine and bromine activation from
1137 artificial saline snow, *Atmos. Chem. Phys.*, 13(19), 9789–9800, doi:10.5194/acp-13-9789-2013, 2013.
- 1138 Yang, X., Pyle, J. A. and Cox, R. A.: Sea salt aerosol production and bromine release: Role of snow on
1139 sea ice, *Geophys. Res. Lett.*, 35(16), 1–5, doi:10.1029/2008GL034536, 2008.
- 1140 Yang, X., Pyle, J. A., Cox, R. A., Theys, N. and Van Roozendaal, M.: Snow-sourced bromine and its
1141 implications for polar tropospheric ozone, *Atmos. Chem. Phys.*, 10(16), 7763–7773, doi:10.5194/acp-10-
1142 7763-2010, 2010.
- 1143 Yang, X., Frey, M., Rhodes, R., Norris, S., Brooks, I., Anderson, P., Nishimura, K., Jones, A. and Wolff,
1144 E.: Sea salt aerosol production via sublimating wind-blown saline snow particles over sea ice:
1145 parameterizations and relevant microphysical mechanisms, *Atmos. Chem. Phys.*, 19, 8407–8424, 2019.
- 1146 Zhu, L., Jacob, D. J., Eastham, S. D., Sulprizio, M. P., Wang, X., Sherwen, T., Evans, J., Chen, Q.,
1147 Alexander, B., Koenig, T. K., Volkamer, R. and Huey, L. G.: Effect of sea salt aerosol on tropospheric
1148 bromine chemistry, *Atmos. Chem. Phys.*, 6497–6507, 2019.
- 1149